RESEARCH ARTICLE

Effect of mixed physical barrier on seawater intrusion and nitrate accumulation in coastal unconfined aquifers

Jun Wang[1,2] · Jun Kong[1,2] · Chao Gao[1,2] · Lvbin Zhou[1,2]

Abstract

Physical barrier has been proven to be one of the most effective measures to prevent and control seawater intrusion (SWI) in coastal areas. Mixed physical barrier (MPB), a new type of physical barrier, has been shown to have higher efficiency in SWI control. As with conventional subsurface dam and cutoff wall, the construction of MPB may lead to the accumulation of nitrate contaminants in coastal aquifers. We investigated the SWI control capacity and nitrate accumulation in the MPB using a numerical model of variable density flow coupling with reactive transport, and performed sensitivity analysis on the subsurface dam height, cutoff wall depth and opening spacing in the MPB. The differences in SWI control and nitrate accumulation between MPB and conventional subsurface dam and cutoff wall were compared to assess the applicability of different physical barrier. The numerical results show that the construction of MPB will increase the nitrate concentration and contaminated area in the aquifer. The prevention and control efficiency of MPB against SWI is positively correlated with the depth of the cutoff wall, reaching the highest efficiency at the minimum effective dam height, and the retreat distance of the saltwater wedge is positively correlated with the opening spacing. We found a non-monotonic relationship between the change in subsurface dam height and the extent of nitrate accumulation, with total nitrate mass and contaminated area increasing and then decreasing as the height of the subsurface dam increased. The degree of nitrate accumulation increased linearly with increasing the height of the cutoff wall and the opening spacing. Under certain conditions, MPB is 46–53% and 16–57% more efficient in preventing and controlling SWI than conventional subsurface dam and cutoff wall, respectively. However, MPB caused 14–27% and 2–12% more nitrate accumulation than subsurface dam and cutoff wall, respectively. The findings of this study are of great value for the protection of coastal groundwater resources and will help decision makers to select appropriate engineering measures and designs to reduce the accumulation of nitrate pollutants while improving the efficiency of SWI control.

Keywords Seawater intrusion · Mixed physical barrier · Cutoff wall · Subsurface dam · Nitrate pollution · Residual saltwater removal

Introduction

Coastal areas are not only the most densely populated regions but also among the most economically active regions in the world. Reportedly, 50–70% of the global population resides in coastal plain areas, which occupy a mere 5% of the Earth's surface (Board and National Research Council 2007). Groundwater is a critical resource for human survival and serves as a primary source of freshwater in coastal areas, providing a vital water source for human activities, such as agriculture and industry. However, human activities, such as excessive use of fertilizers and discharge of domestic and industrial wastewater, have significantly increased the nitrate content in groundwater, leading to severe pollution (Lu and Tian 2017; Fang et al.

✉ Jun Kong
  kongjun999@126.com

1. Key Laboratory of Coastal Disaster and Protection (Hohai University), Ministry of Education, Nanjing, China

2. State Key Laboratory of Hydrology, Water Resources and Hydraulic Engineering, Hohai University, Nanjing, China

2020; Xin et al. 2019, 2021). Nitrate pollution in groundwater is a global environmental concern (Cui et al. 2014; Jang et al. 2017; Nai et al. 2020; Torres-Martínez et al. 2021). Despite the development of various measures to control nitrate pollution in groundwater (Gibert et al. 2019; Hu et al. 2019; Zhang et al. 2019; Zambito Marsala et al. 2021; Gao et al. 2023), effectively controlling the increasing nitrate levels in groundwater remains a persistent and challenging issue.

At the same time, coastal areas are currently facing an increasingly serious threat of seawater intrusion (SWI) (Fig. 1a). Overexploitation of groundwater in these areas has caused a decline in groundwater levels, which, combined with sea level rise caused by global climate change, has made SWI the primary cause of freshwater resource deterioration in coastal aquifers (Werner and Simmons 2009; Rozell and Wong 2010; Werner et al. 2013; Walther et al. 2017). Controlling SWI through effective and reasonable methods is critical for the sustainability of coastal areas and ensuring water availability (Abarca et al. 2013; Lu et al. 2016). Various measures have been proposed to control SWI, including artificial groundwater recharge, hydraulic barrier, air barrier, and physical barrier (Lu et al. 2017; Ebeling et al. 2019; Wang et al. 2020; Wu et al. 2020; Zang and Li 2021). Subsurface physical barrier has become the most popular strategy and have been widely studied due to their low operating costs, high stability, and ability to store fresh groundwater resources (Abdoulhalik and Ahmed 2017; Chang et al. 2019; Wu et al. 2020; Yan et al. 2021). Since the 1980s, subsurface physical barrier has been

used globally (Nawa and Miyazaki 2009; Senthilkumar and Elango 2011). Japan, China, and the USA have built a series of subsurface physical barrier for SWI control with remarkable results (McAnally and Pritchard 1997; Japan Green Resources Agency 2004; Kang and Xu 2017; Zhang et al. 2021). The two main types of physical barrier are subsurface dam and cutoff wall (Abdoulhalik and Ashraf 2017; Gao et al. 2021). Cutoff wall is constructed in the upper part of the aquifer, and groundwater is discharged through openings in the lower part of the aquifer (Fig. 1b). Subsurface dam is built at the bottom of the aquifer, and groundwater is discharged through openings in the upper part of the aquifer (Fig. 1c) (Gao et al. 2021; Sun et al. 2021).

The feasibility of using physical barrier to inhibit SWI has been well established (Abdoulhalik and Ashraf 2017; Shen et al. 2020; Wu et al. 2020). However, the construction of physical barrier, particularly subsurface dam, can hinder the hydraulic connection between upstream and downstream, leading to high concentrations of residual saltwater being trapped behind the dam. As a result, residual saltwater has become a serious problem that limits the development of fresh groundwater in coastal areas. Luyun et al. (2009) showed that the time required to remove residual saltwater in the upstream aquifer after the construction of subsurface dam is considerably longer than the intrusion time of saltwater. Moreover, the removal time of residual saltwater decreases as the height of the dam decreases. At the field scale, Zheng et al. (2020) found that complete desalination
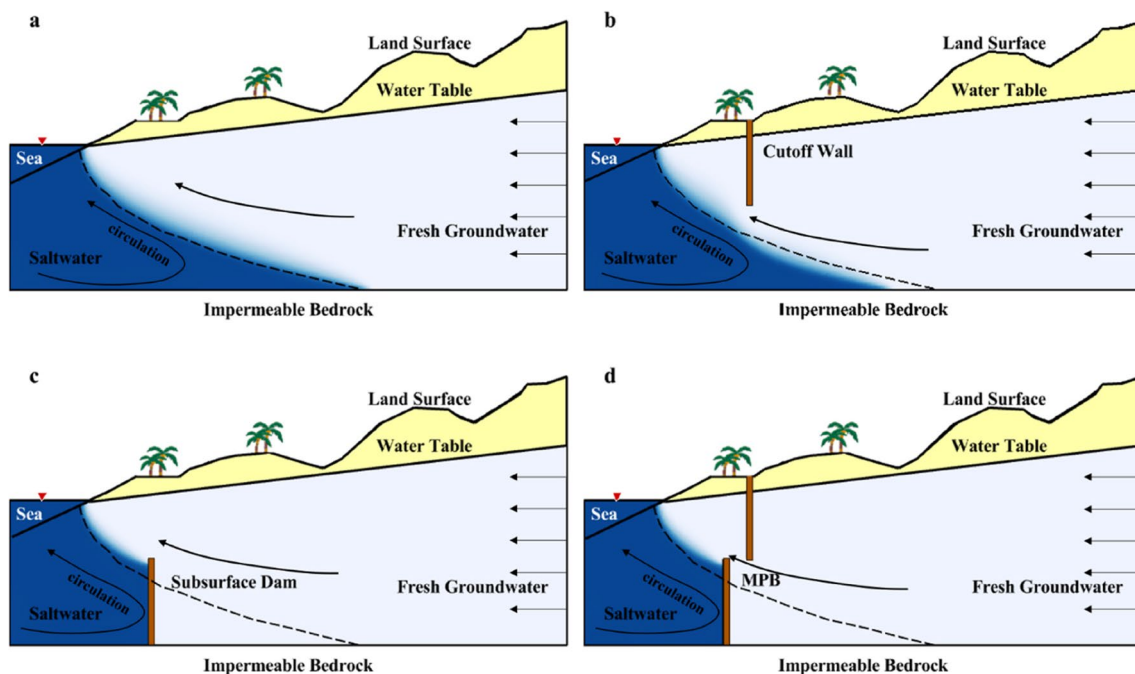

Fig. 1 A schematic diagram of SWI (**a**), cutoff wall (**b**), subsurface dam (**c**), and MPB (**d**). The dashed line indicates the location of the saltwater wedge in the initial stage of SWI, and the dashed area behind the physical barrier represents the residual saltwater area

of residual saltwater trapped upstream of subsurface dam could take several decades, significantly impacting the availability of fresh groundwater. Abdoulhalik and Ashraf (2017) used laboratory tests and numerical techniques to demonstrate that aquifer stratification patterns play a crucial role in determining the effectiveness of subsurface dam in removing residual saltwater. They also found that layered heterogeneity can significantly prolong the cleanup time of residual saltwater compared to homogeneous aquifers.

The construction of physical barrier that obstruct fresh groundwater flow to the ocean may also impact the transport of contaminants in the aquifer, leading to their retention in the aquifer (Gao et al. 2022; Fang et al. 2022). Nitrate has been identified as a major pollutant that poses a threat to freshwater resources and coastal marine ecosystems (Abarca et al. 2013; Anwar et al. 2014). Numerous studies have investigated the impact of physical barrier on nitrate fate in aquifers (Yoshimoto et al. 2013; Kang and Xu 2017) and have confirmed that subsurface physical barrier hinders nitrate discharge to the ocean, exacerbating nitrate pollution of groundwater. For instance, the studies by Yoshimoto et al. (2013) and Kang and Xu (2017) found that the construction of cutoff wall led to a notable increase in the average concentration of nitrate in groundwater. Other studies have examined the influence of factors such as barrier physical parameters, aquifer properties, and nitrate sources on nitrate accumulation in aquifers (Sun et al. 2019, 2021; Ke et al. 2021; Gao et al. 2022). Sun et al. (2019) investigated the factors affecting nitrate emission in aquifers impeded by subsurface dam through experimental and numerical analysis and concluded that wall height and aquifer permeability are the key factors determining nitrate accumulation. Ke et al. (2021) examined the impact of hydraulic gradients, nitrate contaminant source concentrations, relative height and location of subsurface physical barrier, as well as the condition of the physical barrier and cutoff wall on groundwater nitrate contamination. Their results indicated that the hydraulic gradient and the relative height of the subsurface physical barrier was the main factors influencing nitrate accumulation, and that the cutoff wall had a more pronounced effect on nitrate retention than the subsurface dam. Sun et al. (2021) considered the effect of denitrification and investigated the mechanisms by which physical barrier affects SWI and NO_3^- accumulation. They showed that the greater the barrier height, the closer the barrier location to the sea, the greater the concentration of infiltrated nitrate, and the lower the inflowing DOC (dissolved organic carbon) concentration, the greater the degree of nitrate accumulation. Gao et al. (2022) investigated the dynamic mechanisms of nitrate accumulation and denitrification in a layered heterogeneous aquifer situation under the influence of a cutoff wall and showed that the stratification pattern greatly disrupted groundwater flow and significantly increased nitrate accumulation.

Abdoulhalik et al. (2017) recently proposed a new approach to control SWI using a mixed physical barrier (MPB) that combines an impermeable cutoff wall and a semi-permeable subsurface dam (Fig. 1d). Gao et al. (2021) investigated the effect of a more realistic MPB, which combines impermeable cutoff wall and subsurface dam, on residual saltwater removal based on approach of Abdoulhalik et al. (2017). Their results showed that MPB is 40%-100% and 0%-56% more effective in removing residual saltwater than conventional subsurface dam and cutoff wall, respectively. MPB has great potential for protecting coastal freshwater resources from SWI. However, the study of Gao et al. (2021) on residual saltwater removal by MPB was limited to a few tens of centimeters, and the total removal process lasted only a few hours. This is not representative of reality, as the natural removal time of residual saltwater often extends from years to decades. Furthermore, previous studies have only examined the mechanisms of the effects of single cutoff wall and subsurface dam on nitrate pollution accumulation. The process of NO_3^- accumulation in aquifers due to MPB construction remains unclear (Fig. 2).
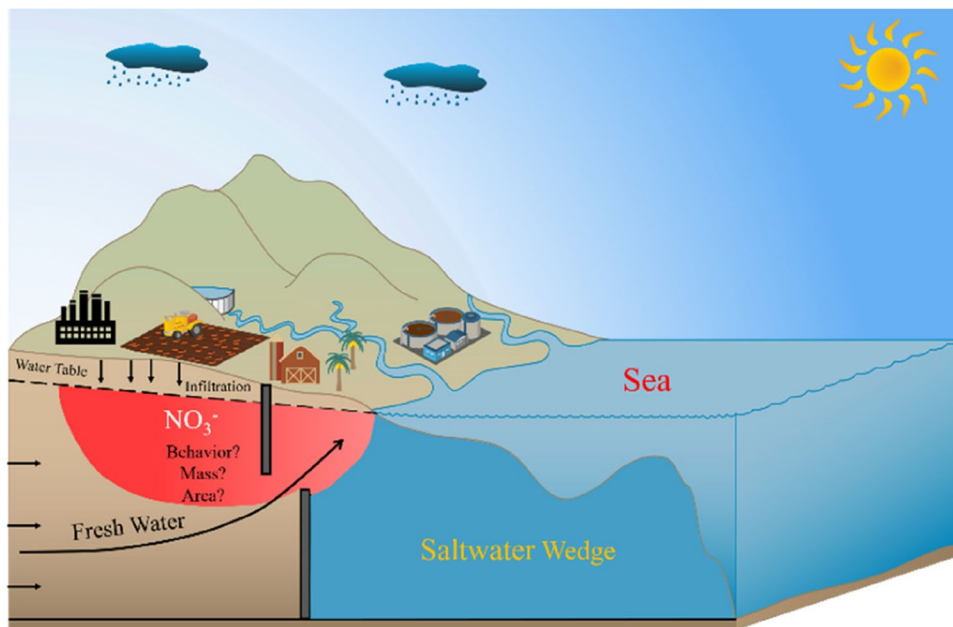
This study investigated the SWI control performance of MPB and their effects on NO_3^- accumulation in aquifers using numerical simulations. The specific objectives were (1) to assess the performance of MPB in preventing and controlling SWI by measuring residual saltwater removal efficiency and saltwater wedge reduction rate; (2) to compare and analyze the differences in total NO_3^- and contaminated area in coastal aquifers before and after MPB installation; (3) to evaluate the impact of MPB structure variables on SWI control performance and NO_3^- accumulation mechanisms; and (4) to compare the differences between MPB and traditional single physical barrier in terms of SWI control performance and NO_3^- pollution accumulation effects. These results will assist decision-makers in selecting appropriate engineering measures and barrier types during physical barrier construction to safeguard subsurface freshwater resources in coastal areas.

Methods

Governing equations

In this study, we utilized the finite element software COMSOL Multiphysics to establish a two-dimensional variable-density flow and reactive transport model. This model simulated the variable-density groundwater flow, salt transport, and reactive solute transport in unconfined coastal aquifers under static oceanic boundary conditions. The model couples unsaturated porous medium flow, based on the Richards equation, with solute transport, based on the convection–dispersion-reaction equation:

Fig. 2 A schematic diagram of saltwater intrusion and nitrate contamination in a homogeneous coastal unconfined aquifer with MPB

$$\rho\left(S_e S + \frac{C_m}{\rho g}\right)\frac{\partial p}{\partial t} + \nabla \cdot \rho\left(\frac{-k_s}{\mu}k_r(\nabla P + \rho g \nabla Z)\right) = Q_m \tag{1}$$

$$\frac{\partial(\theta C_i)}{\partial t} + \nabla \cdot \rho\left(\frac{-k_s}{\mu}k_r(\nabla P + \rho g \nabla Z)C_i\right) = \nabla \cdot (D\nabla C_i) + R_i \tag{2}$$

where ρ is the fluid density; S_e denotes the effective saturation, which is related to the pore water pressure (Eq. 7); S denotes the water storage coefficient; C_m is the specific moisture capacity, which is related to the variation of water content (Eq. 5); k_s is the permeability of the sediment at full saturation calculated from the hydraulic conductivity coefficient (K) (Eq. 3); k_r is the relative permeability depending on the effective saturation Se (Eq. 4); μ is the hydrodynamic viscosity; P and Z are the pressure and elevation, respectively; g is the acceleration of gravity; Q_m is the fluid mass source term that is related to the tidal effect; θ is the water content; C_i is the solute concentration of species i; D is the hydrodynamic dispersion tensor; and R_i is the reaction rate of the ith reactant. The sediment storage properties caused by the compressibility of water and solid substrates and the additional source/sink terms generated by tidal load effects are neglected in Eq. 1 (Reeves et al. 2000; Wilson and Gardner 2006).

The numerical model utilized the Van Genuchten (1980) model to establish the intrinsic correlations between the relative permeability (k_r), specific moisture capacity (C_m), effective saturation (S_e), and pore water pressure (P):

$$k_s = \frac{\mu K}{\rho g} \tag{3}$$

$$k_r = S_e^{0.5}\left(1 - \left[1 - S_e^{1/m}\right]^m\right)^2 \tag{4}$$

$$C_m = \frac{\alpha m}{1-m}(\theta_s - \theta_r)S_e^{1/m}\left[1 - S_e^{1/m}\right]^m \tag{5}$$

$$\theta = \theta_r + S_e(\theta_s - \theta_r) \tag{6}$$

$$S_e = \frac{1}{(1 + |\alpha P|^n)^m} \tag{7}$$

$$m = 1 - \frac{1}{n} \tag{8}$$

where θ_s and θ_r are the saturated liquid volume fraction and residual liquid volume fraction, respectively; the intrinsic relationship constants α and n are derived from the study conducted by Shen et al. (2019).

In the mixing process of salt and fresh water, the density of pore water varies with the salt concentration in the pore water, and the fluid density is based on the density function of salinity C in the pore water is expressed as follows.

$$\rho = \rho_f + \frac{\partial \rho}{\partial c}C \tag{9}$$

where ρ_f is the density of freshwater, taken as 1000 kg/m³; $\partial\rho/\partial C$ is the rate of change of fluid density, taken as 0.7143; C is the salinity of pore water.
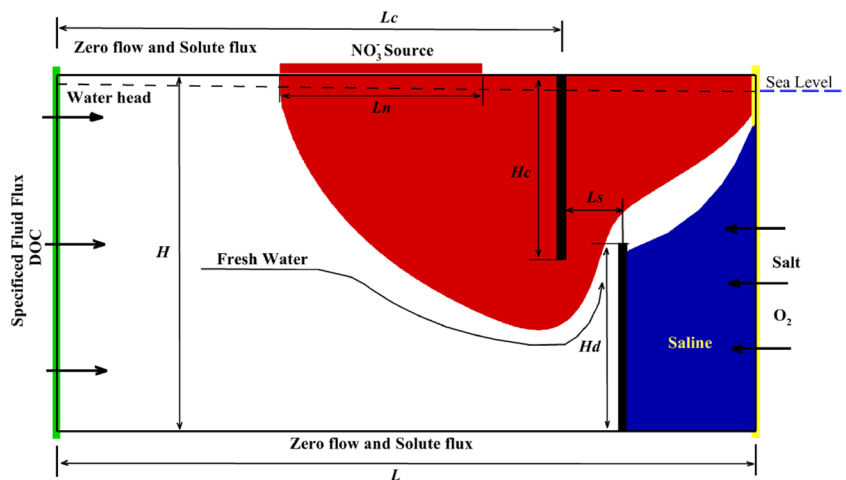
Model setup

Groundwater flow and salt transport model

The model area represents a cross section of a two-dimensional homogeneous beach aquifer, as shown in Fig. 3. The boundary conditions of groundwater flow and salt transport model were set to simulate the natural forcing conditions acting on the beach aquifer. The aquifer is assumed to be located on bedrock, and the aquifer basement is considered impermeable with no flow boundary and zero salt flux boundary. The freshwater boundary on the left is a constant flow and salt concentration boundary with a flow rate of 0.4 m³/day (Q_f) and a salt concentration of 0 ppt. Infiltration zones with a constant salt concentration of 0 ppt were established along specific areas of the upper boundary, with the infiltration zone length (Ln) and infiltration rate (R) based on Sun et al. (2019, 2021). Other permanently exposed upper surfaces were set up as no-flow boundaries and zero salt flux boundaries, without considering precipitation and evaporation effects. The seaward boundary on the right is a permeable boundary with an external head equal to the sea level head and an open boundary with an external concentration equal to seawater salt concentration. The boundary condition is specified by the following equation:

$$-n_f \cdot \rho \frac{-k_s}{\mu} k_r(\nabla P + \rho g \nabla Z) = \rho R_b (H_w - H_b) \tag{10}$$

$$R_b = \frac{K}{D_l} \tag{11}$$

$$C = C_{sea} \quad n_f \cdot u < 0 \tag{12}$$

$$-n_f \cdot D\nabla C = 0 \quad n_f \cdot u \geq 0 \tag{13}$$

where n_f is the normal vector of the boundary; R_b is the conductivity, defined as the ratio of the hydraulic conductivity coefficient K to the coupling length scale D_l; H_b is the sea level head and H_w is the groundwater head.

Equations 10 and 11 reveal that (1) when H_b is higher than H_w under saturated conditions, the head difference between the overlying surface water and the interfacial sediment will determine the water flux at the boundary; (2) under saturated conditions, when H_b is lower than or equal to H_w, a seepage surface forms along this boundary (Abarca et al. 2013; Chui and Freyberg 2009); and (3) under unsaturated conditions, when the pressure head is less than 0, the conductivity value (R_b) is set to 0, causing the boundary to become a no-flow boundary (Chui and Freyberg 2009).

Salt transport at the open boundary is determined by the direction of groundwater flow at the boundary, as indicated by Eqs. 12 and 13. Specifically, nodes flowing into the aquifer are assigned a seawater concentration of 35 ppt, while nodes flowing out of the aquifer have a zero-concentration gradient (Cardenas et al. 2015; Shen et al. 2019).

The physical barrier is simulated by setting specific areas as inactive units. The subsurface dam and cutoff wall thickness are fixed at 0.6 m, while the depth, height, and opening spacing of the MPB are variable and denoted by Hc, Hd, and Ls, respectively. Table 1 lists the model parameters related to groundwater flow and salt transport. The simulation area measures 90×23 m² and is discretized by a uniform grid with a size of $\Delta x \times \Delta y = 0.3$ m $\times$ 0.25 m. This grid spacing satisfies the Péclet number criterion, ensuring that the mathematical model is numerically stable. The Péclet number is defined as follows (Voss & Souza 1987):

Fig. 3 Area and boundary of numerical simulation. H and L are the height and length of the simulated area. Hc, Hd, Ls, Lc, and Ln represent the depth of cutoff wall, the height of subsurface dam, MPB opening spacing, spacing between MPB and landside boundary, and length of NO_3^- infiltration zone, respectively

Table 1 Summary of model numerical parameters

Parameters	Description	Value	Units
Hc	Depth of cutoff wall	0, 9, **11**, 13, 15, 17	m
Hd	Height of subsurface dam	0, 8, 10, **12**, 14, 16	m
Ls	Opening spacing of MPB	4, 6, **8**, 10	m
Lc	Cutoff wall location	65	m
Aquifer properties			
L	Model field length	90	m
H	Model field height	23	m
Ln	NO_3^- infiltration zone length	25	m
K^a	Hydraulic conductivity	1.447×10^{-4}	m/s
Φ^a	Porosity	0.45	-
θ_r^a	Residual water volume fraction	0.045	-
θ_s^a	Saturated water volume fraction	0.45	-
n^a	Pore size distribution index	14.5	-
α^a	Inverse of air entry suction parameter	2.68	1/m
α_L^a	Longitudinal dispersivity	0.4	m
α_T^a	Transverse dispersivity	0.04	m
ρ_s	Seawater density	1025	kg/m^3
ρ_f	Freshwater density	1000	kg/m^3
Hs	Mean sea level	22	m
Q_f	Inland fresh groundwater flux	0.4	m^3/day
R	NO_3^- infiltration rate	0.03	m/day
C_S	Seawater concentration	35	ppt
C_L	Freshwater concentration	0	ppt
D_l^b	Coupling length scale	0.001	m
Reactant boundary concentration			
C_N^c	Infiltration NO_3^- concentrations	100	mg/L
C_O^c	Infiltration O_2 concentrations	0.2	mM
C_D^c	Infiltration DOC concentrations	1	mg/L
Kinetic parameter values			
Kfox^c	Rate constant for decomposition of DOC	1.5×10^{-6}	1/s
KmO$_2^c$	Limiting concentration of dissolved oxygen	3.125×10^{-5}	M
KmNO$_3^{-c}$	Limiting concentration of NO_3^-	8.065×10^{-6}	M

The numbers in bold are the reference values for Hc, Hd, and Ls

[a]Shen et al. (2019)

[b]Shoushtari et al. (2015)

[c]Heiss et al. (2017)

$$Pe_m \approx \frac{\Delta x}{\alpha_L} = 0.75 < 4 \qquad (14)$$

where Δx is the grid size in the x-axis direction and α_L is the dispersion coefficient in the x-axis direction.

Reaction transport model

Reactive solute transport in the aquifer is calculated based on the velocity field of the variable density groundwater flow model. The bottom of the model domain (Fig. 3) is subject to a flux-free boundary condition. Specific areas along the upper boundary are designated as NO_3^- permeability zones,

with NO_3^- concentration (C_N) in the zones based on Sun et al. (2019, 2021). The remaining upper surface is subject to no-flow and zero-flux boundaries. The land side of the simulation area is subject to a constant concentration boundary condition. Similar to the salt transport model, an open boundary on the seaward side (right-hand side in Fig. 3) specifies an external concentration equal to the solute concentration in seawater. Seawater entering the simulated area through the aquifer-ocean interface is the source of O_2, while DOC is present in fresh groundwater inflow from the land boundary, as shown in Fig. 3.

The aerobic respiration and denitrification processes involved in this model follow Heiss et al. (2017) and Bardini

Table 2 Reaction and kinetic rate expressions (using Bardini et al. 2012; Heiss et al. 2017)

Name	Reaction	Rate expression
Oxic degradation	$DOC + O_2 \rightarrow CO_2 + H_2O$	If $[O_2] > KmO_2$; rate $= Kfox[DOC]$
		If $[O_2] < KmO_2$; rate $= Kfox[DOC][O_2]/KmO_2$
Denitrification	$5DOC + 4NO_3^- + 4H^+ \rightarrow 5CO_2 + 7$ $H_2O + 2N_2$	If $[O_2] > KmO_2$; rate $= 0$
		If $[O_2] < KmO_2$ and $[NO_3^-] > KmNO_3^-$; rate $= Kfox[DOC](1\text{-}[O_2]/KmO_2)$
		If $[O_2] < KmO_2$ and $[NO_3^-] < KmNO_3^-$; rate $= Kfox[DOC](1\text{-}[O_2]/KmO_2)$ $[NO_3^-]/KmNO_3^-$

Table 3 Parameter values used for the sensitivity analysis simulation cases

No	Hd	Hc	Ls	Note
1	-	-	-	Case A
2	12	11	8	Case B
3	8	11	8	Sensitivity to Hd
4	10	11	8	
5	14	11	8	
6	16	11	8	
7	12	9	8	Sensitivity to Hc
8	12	13	8	
9	12	15	8	
10	12	17	8	
11	12	11	4	Sensitivity to Ls
12	12	11	6	
13	12	11	10	

et al. (2012). The aerobic respiration and denitrification reaction networks and their kinetic equations are shown in Table 2, and the reactant concentrations and reaction kinetic parameter values are shown in Table 1.

A fully coupled solver is used to solve the multi-physics field coupled equations, which simultaneously solve for groundwater flow, solute transport, and reactions. The simulation consists of four steps: First, groundwater flow and salt transport are calculated without a physical barrier and with an initial value of 0 until the steady-state head and salt concentration are achieved. Second, using the steady-state results from the first step as initial values, the SWI removal process is calculated with the installation of physical barrier. Third, the initial value of reactive solute concentration is set to 0, and 2000 days of variable density water flow and non-reactive transport of multiple solutes are simulated to ensure steady-state head and solute concentration. Finally, the reaction rate of the reactive solute is added to the results of the third step to simulate another 2000 days until the reactive solute reaches equilibrium.

This study compared the effect of the MPB on SWI and nitrate accumulation by first considering the no physical barrier case (case A) and the base case (case B). Next, a sensitivity analysis was conducted based on case B to explore the effects of variations in the height, depth, and opening spacing of MPB on SWI and nitrate accumulation. Table 3 summarizes the simulated cases for the sensitivity analysis. Finally, to determine the value of MPB applications, the differences in SWI control performance and nitrate accumulation between the MPB and single physical barrier (subsurface dam and cutoff wall) were compared.

Measurable diagnostics

To assess the effectiveness of physical barrier in SWI control performance, two dimensionless parameters were introduced: the saltwater wedge length reduction rate (R_S) and the post-barrier residual saltwater removal rate (R_M). R_S and R_M are expressed as, respectively:

$$R_S = \frac{L_0 - L_f}{L_0} \tag{15}$$

$$R_M = \frac{M_0 - M}{M_0} \tag{16}$$

where L_0 is the initial length of the saltwater wedge before MPB installation and L_f is the length of the saltwater wedge after MPB installation. M_0 is the initial residual total salt mass trapped in the inland aquifer before MPB installation. M_0 is constant for a dam installed at a fixed position while it has various values for dams installed at different positions. M is the residual total salt mass in the inland aquifer after MPB installation. A seawater salinity of 0.5 ppt was used as a threshold to define the total amount of saltwater water behind the barrier, and the toe location was determined by the isoline of 50% seawater salinity.

To compare the effect of physical barrier on nitrate accumulation in aquifers, two parameters were used: the total nitrate mass accumulation rate (*TNM*) and the nitrate contaminated zone area increase rate (*VNM*). The *TNM* and *VNM* are described below:

$$TNM = \frac{TNM_W}{TNM_N} \tag{17}$$

$$VNM = \frac{VNM_W}{VNM_N} \qquad (18)$$

where TNM_W and VNM_W are the total nitrate amount and nitrate contaminated area of the aquifer after physical barrier installation, respectively, and TNM_N and VNM_N are the total nitrate amount and nitrate contaminated area of the aquifer before physical barrier installation. According to WHO standards, a NO_3^- concentration of 11.3 mg/L is used as a threshold to define the nitrate pollution zone.

Results

NO_3^- accumulation under MPB

Figure 4 shows the steady-state cross-sectional distributions of salinity, NO_3^- concentration, and DOC concentration in the aquifer under two conditions: no physical barrier installation (case A) and MPB installation (case B). Without physical barrier, a saltwater wedge about 57 m long was formed along the bottom of the aquifer side against the sea due to the difference in density and hydraulic gradient of salty and freshwater. The subsurface fresh water moved upward under the effect of buoyancy and eventually sank into the ocean. NO_3^- seeping from the surface formed a semi-elliptical pollution zone in the aquifer, while the distribution of DOC entering the aquifer from the landside boundary was

limited by the saltwater wedge and NO_3^-, and most of it was consumed by denitrification and oxidation reactions. When the MPB was constructed, the toe of the saltwater wedge receded to the location of the subsurface dam, and the subsurface freshwater sank into the ocean through the opening between the subsurface dam and the cutoff wall. Compared to case A, the NO_3^- contaminated area and the total NO_3^- mass on the left side of the subsurface dam increased significantly, especially in the deeper part of the aquifer. However, the NO_3^- contamination above the subsurface dam decreased slightly due to the increased flow velocity in the vertical direction, which inhibited the downward transport and diffusion of NO_3^-. The DOC in the deep part of the aquifer pushed toward the ocean and filled the lower part of the aquifer due to the retreat of the saltwater wedge toward the ocean.

We used the metrics TNM, TNM', VNM, and VNM' (where TNM' and VNM' denote TNM_W, TNM_N, and VNM_W, VMN_N) to quantify the effect of the MPB on NO_3^- accumulation in case A and case B. Figure 5a demonstrates the evolution of TNM and TNM' over time for both cases. Prior to considering biochemical reactions, TNM' gradually increased until it reached a steady state as vertical infiltration of NO_3^- occurred, which resulted in values of 48.21 kg and 63.42 kg for case A and case B, respectively. At stabilization, the TNM index was approximately 31.57%. Throughout the experiment, TNM rapidly increased, followed by a slow decrease before gradually increasing and stabilizing at

Fig. 4 Cross-sectional distributions of salinity, NO_3^- and DOC for the case without physical barrier (case A) and the case with MPB installed (case B), the distributions for each case are shown in the left and right columns, respectively. The arrows indicate the flow direction and velocity magnitude. Purple, green, and yellow colors indicate the 10%, 50%, and 90% salinity contours, respectively. The white columns are the subsurface dam and cutoff wall of the MPB, which are 17 m and 25 m from the sea-side boundary, respectively. Realistic scales are used for the length units in [m]
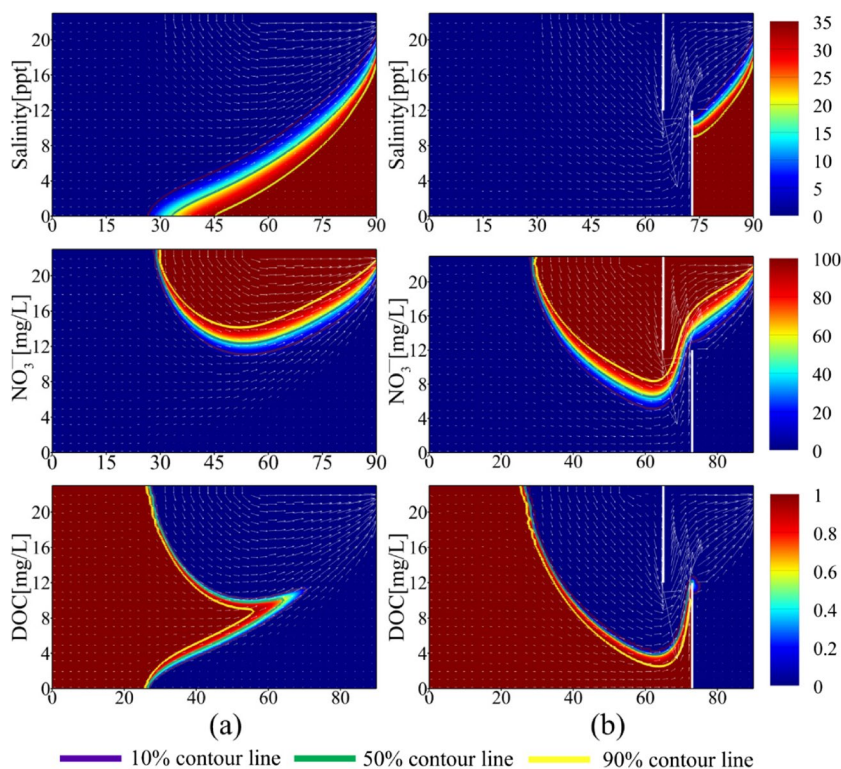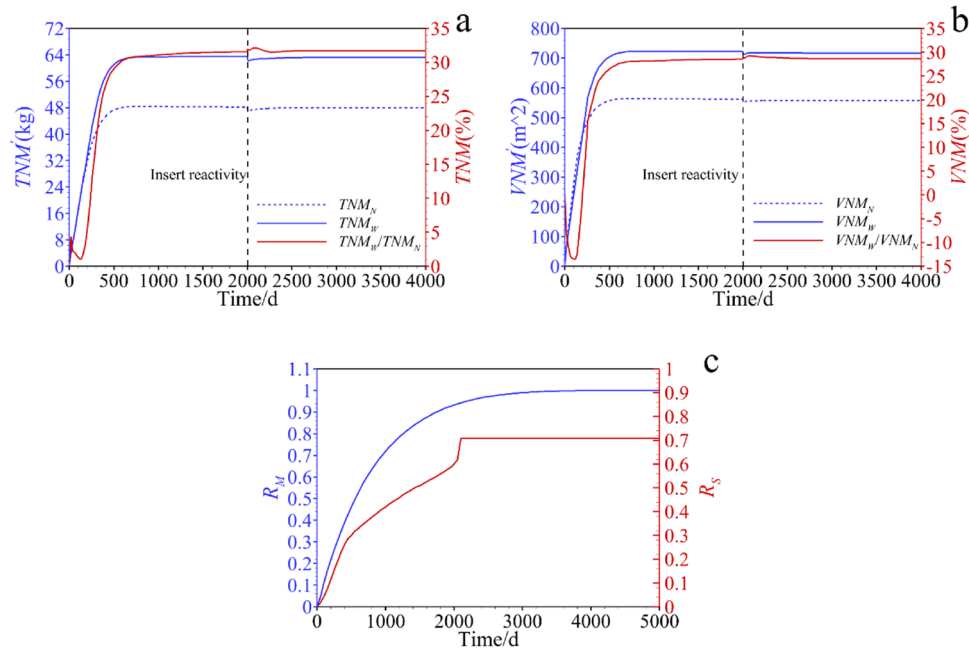
Fig. 5 **a** Non-reactive transport and reactive transport simulation phases, total nitrate mass (TNM_N, TNM_W) and TNM (red solid line) versus time. **b** Non-reactive transport and reactive transport simulation phases, nitrate contaminated area (VNM_N, VNM_W) and VNM (red solid line) versus time. **c** Time-varying processes of R_S (red solid line) and R_M (blue solid line) during the simulation phase of residual saltwater removal. In **a** and **b**, the blue solid lines represent TNM_W and VNM_W for case B, respectively. In **a** and **b**, the blue dashed lines represent TNM_N and VNM_N for case A, respectively. The changes of each index with time before and after reaction is considered are denoted by the left and right sides of the black dashed lines in **a** and **b**, respectively

a steady state. TNM was always greater than zero during the entire process, indicating that MPB facilitated NO_3^- accumulation. After biochemical reactions were coupled, total NO_3^- went through a short decline phase due to mass consumption but ultimately returned to a stable phase. This caused the TNM' values for Case A and Case B to slightly decrease to 48.0 kg and 63.22 kg, respectively, compared to their pre-reaction counterparts. Meanwhile, TNM was slightly larger after considering biochemical reactions, reaching 31.69%.

Figure 5b displays the transient processes of VNM and VNM' over time in the aquifers of case A and case B from the initial conditions to reaching a steady state. Before considering the reaction, the size of the contaminated zone, VNM', increases with time until it reaches a steady state. In the early stage of NO_3^- infiltration (the first 250 days), the growth rate and value of VNM' in case A were slightly larger than in case B. This was due to the interception wall in case B blocking the transport diffusion of NO_3^- in the horizontal direction and the slower increase in the transport rate of NO_3^- in the vertical direction in the initial stage. With continued NO_3^- infiltration, the growth rate and value of VNM' in case B gradually became larger than in case A until it reached a steady state. After stabilization, the VNM' of case A and case B were 562.02 m² and 722.45 m², respectively, and the VNM was stabilized at 28.8%. After considering the

consumption of NO_3^- by the reaction, the NO_3^- contaminated area in the aquifer underwent a brief decline phase at the beginning, but then returned to the stabilization phase after 1000 days. The stabilized VNM' were 557.48 m² and 716.99 m², respectively, and the VNM was equal to 28.61%.

The processes of TNM, TNM', VNM, and VNM' indicate that nitrate pollution growth in the aquifer follows similar trends in both cases. However, installing MPB inhibits the seaward discharge of NO_3^-, increases the total amount of NO_3^- in the aquifer, expands the NO_3^- pollution zone, leads to more severe nitrate accumulation, and deteriorates the subsurface freshwater resources.

SWI control performance

The saltwater removal process is calculated after installing the MPB while assuming that the barrier installation is transient and does not affect the initial pressure and salinity distribution of the aquifer. Figure 5c displays the variation process of R_M and R_S over time after the installation of MPB. During the period from the initial moment to day 600, R_M increases to over 50% as a nearly linear function, and its rate of increase gradually slows down after day 600. After approximately 1200 days of MPB installation, the R_M value increases to over 70% and then increases at a decreasing rate until it reaches stability on day 4650. The R_S

increased rapidly during the first period of saline clearance (first 400 days), after which its growth rate gradually diminished until day 2100 when there was an abrupt change in the growth rate, and the R_S rapidly increased in a short period of time before reaching stability on day 2200. The sudden change in the R_S growth rate in the later stage is mainly due to the disappearance of the 50% salinity contour behind the dam when the saline water decreases to a certain level, and the salinity contour is truncated due to the non-existence of salinity in the area where the subsurface dam is located.

Figure 6 illustrates the concentration distribution of residual saltwater at different stages after MPB installation. Once SWI has occurred, saturated aquifers can typically be divided into saline, freshwater, and mixed zones. The mixing zone is the transition zone between brackish and freshwater areas, and when the salinity of seawater is standard salinity, the area with salinity between 10 and 90% is generally considered to belong to the mixing zone (Lu & Luo 2010; Lu et al. 2009). We divided the mixing zone into a high salinity mixing zone (HCMZ) with a salinity range of 50 to 90% and a low salinity mixing zone (LCMZ) with a salinity range of 10 to 50% (Zheng et al. 2020). The LCMZ is the primary channel for saltwater discharge, and the efficiency of saltwater desalination behind the dam is dominated by the concentration gradient between the LCMZ and HCMZ and the LCMZ at the dam with respect to the dam height, which is dominated by the relative height. As shown in Fig. 6, the area of the mixing zone near the subsurface dam and the toe of the

saltwater wedge increased significantly during the initial period after MPB installation (day 200). The 10% salinity contour moved upward at the location of the subsurface dam and to the right of the dam, and was depressed to the left of the dam, with no significant change in the location of the 10% contour at the salt toe. The 50% and 90% salinity contours experienced significant retreat. At days 600 and 1200 after MPB installation, the mixing zone area decreased relative to the initial moment, but the 10% salinity contour remained higher than the subsurface dam, and the 10%, 50%, and 90% salinity contours all experienced significant retreat. On day 2000 after MPB installation, the HCMZ almost disappeared, and only a small amount of low concentration saltwater was retained upstream, with the 10% salinity contour level with the top part of the subsurface dam, and its 10% and 50% salinity contours receded significantly less relative to the first 1200 days.

The analysis demonstrates that the desalination mechanism of MPB is in line with the proposals of Zheng et al. (2020) and Gao et al. (2021). That is to say, when the HCMZ is large and the LCMZ exceeds the dam, the salt in the HCMZ is dispersed into the LCMZ at a faster rate, while low concentration saltwater is more easily discharged across the dam to the sea boundary, resulting in higher desalination efficiency and quicker decay of residual saltwater mass and area. However, when only a small amount of low concentration saltwater is retained behind the dam and the 10% salinity contour is lower than the dam, the rate of internal salt dispersion to the outside is

Fig. 6 Distribution of saline wedge at 0, 200, 600, 1200, 2000, and 4000 days after installation of MPB (case A). The white columns are the subsurface dam and cutoff of MPB, which are 17 m and 25 m from the sea-side boundary, respectively. Purple, green, and yellow solid lines represent the salinity contours of 10%, 50%, and 90% of seawater, respectively
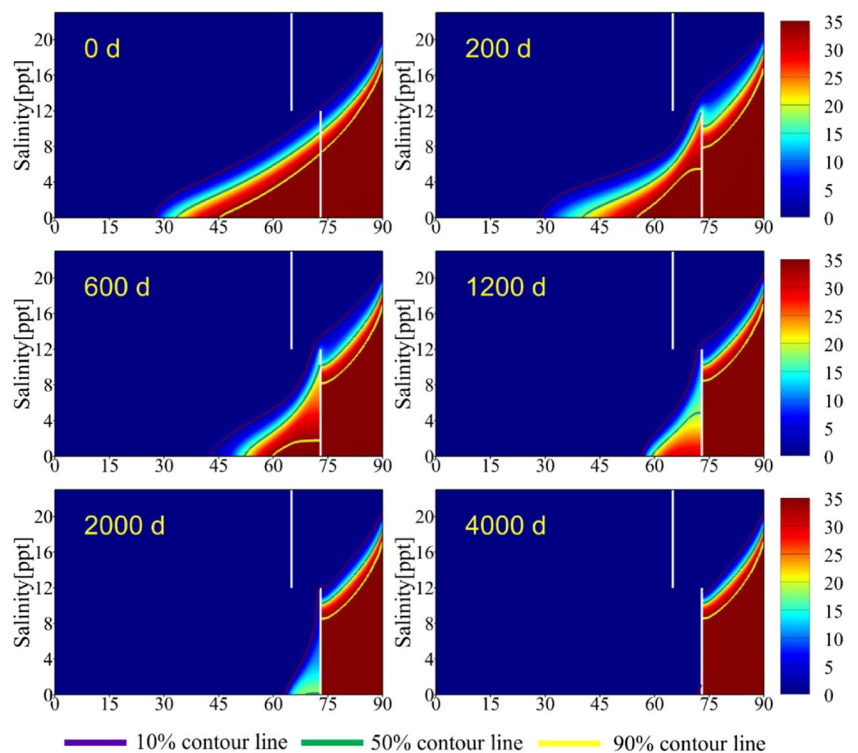
greatly reduced, and the saltwater needs to flow vertically from the bottom to the top of the dam. Therefore, the saltwater removal rate decreases significantly, and the residual saltwater quality and area decay slowly.

Discussions

## Influences of subsurface dam height

In this subsection, we simulated a series of MPB cases with varying subsurface dam heights (Table 3) while

maintaining Hc and Ls at the same levels as the base case (case B). The objective was to study how the subsurface dam height, Hd, affects the performance of SWI control and the extent of NO_3^- accumulation.

Nitrate accumulation

Figure 7 illustrates the distributions of nitrate and DOC for different subsurface dam heights (Hd) at steady state. As shown in Fig. 7, the height of the subsurface dam has some effect on the distribution of NO_3^-. As Hd increases, the depth of the nitrate pollution zone on the left side of

Fig. 7 Cross-sectional distribution of salinity, NO_3^- and DOC for MPB using different subsurface dam heights under stable conditions. The purple, green and yellow colors indicate the concentration contours of 10%, 50%, and 90%, respectively. The white bars are the subsurface dam and cutoff wall of the MPB, which are 17 m and 25 m from the sea-side boundary, respectively. Realistic scales are used for the length units in [m]
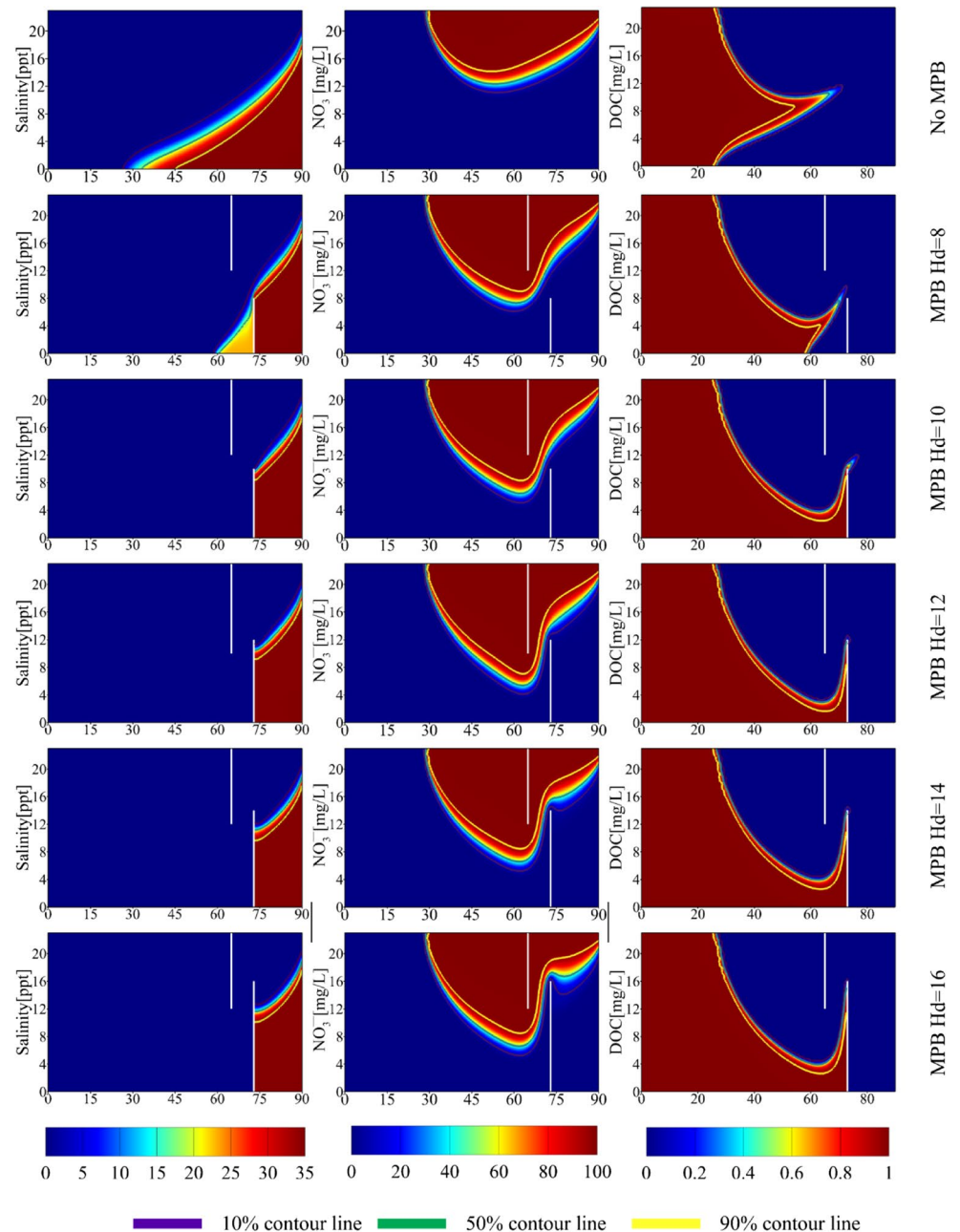
the MPB opening (as indicated by the 10% concentration contour position) gradually increases. When $Hd = 12$ m, the depth of nitrate pollution is at its maximum, and when $Hd \geq 12$ m, the depth of the nitrate pollution zone gradually decreases. The area of the nitrate mixing zone (10 to 90% concentration contour range) on the left side of the opening does not show significant changes due to the increase in Hd. Above the subsurface dam, the depth of nitrate contamination decreases in steps with increasing Hd. The relationship between nitrate distribution on the right side of the opening and Hd is different from that on the left side. The 90% concentration contour on the right side of the opening shifts upward with increasing dam height, while the 10% and 50% concentration contours are depressed near the subsurface dam, and the depth of the depression is proportional to Hd. The area of the nitrate mixing zone on the right side of the opening changes significantly with increasing Hd, and the area of the mixing zone increases with increasing Hd. Figure 8a and b show the effect of Hd of MPB on nitrate accumulation. The TNM values for subsurface dam heights of 8 m, 10 m, 12 m, 14 m, and 16 m were 30.02%, 33.58%, 31.69%, 29.31%, and 26.77%, respectively, corresponding to VNM values of 27.35%, 30.07%, 28.61%, 27.02%, and 25.69%, respectively. From Fig. 8a and b, it can be observed that when Hd is below 10 m, TNM and VNM gradually increase with increasing Hd. When Hd exceeds 10 m, TNM and VNM gradually decrease. Overall, it exhibits a trend of initially increasing and then decreasing. The reasons for this trend may be as follows: (1) when MPB fails to effectively control SWI, the depth of nitrate transport is limited by the residual saltwater. However, when Hd increases to 10 m, the residual saltwater is completely removed, resulting in a significant increase in the depth of nitrate transport, and the amount of nitrate in the region to the left of the MPB

increases. Although the Hd increase causes a decrease in the nitrate amount on the right side of the MPB, the overall increase in nitrate exceeds the decrease. Thus, both the R_M and R_S values gradually increase as Hd increases from 8 to 10 m. (2) Once Hd exceeds 10 m, the amount of nitrate pollution in the left region of the MPB is primarily controlled by the cutoff wall, and the increase in Hd does not significantly affect the nitrate quantity in this area. However, the nitrate quantity on the right side of the MPB decreases with the Hd increase, especially in areas with high nitrate concentrations. Therefore, when Hd exceeds 10 m, both the R_M and R_S values gradually decrease with the Hd increase.

SWI control performance

Figure 7 shows that when the height of the lower dam is 8 m, the barrier fails to completely control the SWI, and residual saltwater still exists behind the dam. When the dam height is greater than 8 m, the SWI can be effectively controlled. Figure 8c and d illustrate the course of R_M and R_S with time for different dam heights, respectively. When Hd exceeds 8 m, the R_M values gradually increase with time until the residual saltwater inland is completely removed ($R_M = 1$), and the rate of increase gradually decreases with time. When $Hd = 8$ m, the R_M value still increases gradually with time, but the residual saltwater behind the dam cannot be completely removed (as shown in Fig. 7), and the R_M finally stabilizes at 0.84, indicating that the barrier cannot effectively control the SWI. When MPB can effectively control SWI, the R_M growth rate decreases with increasing dam height, and the time for complete removal of residual saltwater increases with increasing dam height. For instance, after 1000 days of MPB installation, the R_M values for subsurface dam heights of 10 m, 12 m, 14 m, and 16 m were

Fig. 8 **a** Variation of TNM, the accumulation rate of total nitrate mass in the aquifer, with subsurface dam height, and Hd equals 0 corresponding to case A. **b** Variation of VNM, the increase rate of nitrate contaminated area in the aquifer, with subsurface dam height, and Hd equals 0 corresponding to case A. **c** Post-barrier residual salt removal rate R_M versus time using MPB with different subsurface dam heights. **d** Saltwater wedge length reduction rate R_S versus time using MPB with different subsurface dam heights
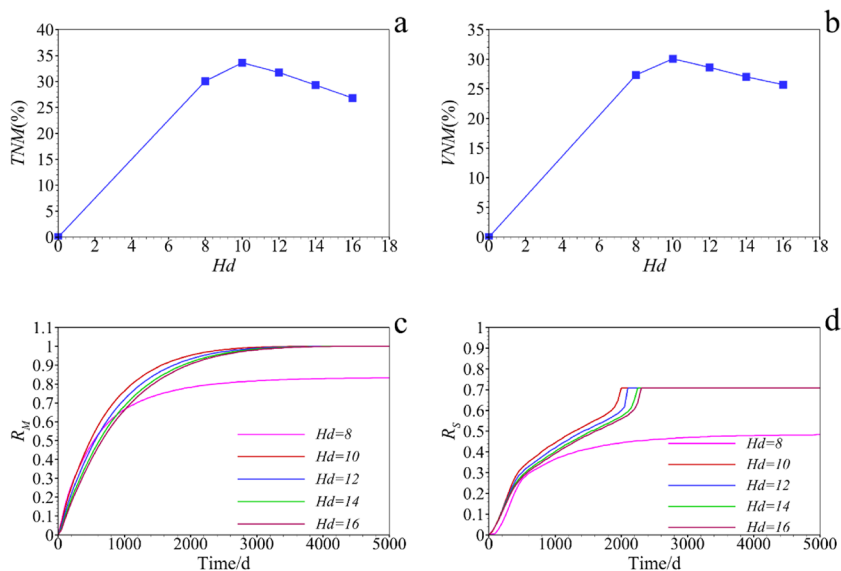
0.76, 0.72, 0.68, and 0.66, respectively, corresponding to complete residual saltwater removal times of 4050, 4650, 4850, and 5000 days, respectively. The R_S values follow a similar pattern to R_M. When Hd is greater than 8 m, R_S values increase with time and eventually reach a stable value of 1.0 (where the 50% salinity contour corresponds to the salt toe reaching the location of the subsurface dam), and when Hd is equal to 8 m, R_S eventually stabilizes at 0.49. The rate of increase of R_S decreases with increasing Hd, and the elapsed time for the salt toe to reach the location of the subsurface dam increases with increasing dam height. The increased height of the subsurface dam lengthens the residual saltwater removal time due to the extended transport path of salts in the low salinity zone. The difference in the variation of R_M and R_S values for different dam heights indicates that the SWI can be effectively controlled only when the dam height of MPB is slightly higher than the 50% salinity contour, and at this time, the residual saltwater removal efficiency is optimal.

Influences of cutoff wall depth

To investigate the effect of cutoff wall depth on SWI and NO_3^- accumulation, a series of MPB cases with different cutoff wall depths (Hc values) were simulated while keeping Hd and Ls the same as the base case (case B) (as shown in Table 3).

Nitrate accumulation

Figure 9 displays the distributions of nitrate and DOC for different cutoff wall depth (Hc) conditions at steady state. As shown in Fig. 9, the range of NO_3^- and DOC distribution is greatly affected by the depth of the cutoff wall. As Hc increases, the depth reached by the nitrate contamination zone on the left side of the opening (10% concentration contour position) gradually increases, and the area of DOC distribution near MPB decreases. The area of the nitrate mixing zone on the left side of the opening (10 to 90% concentration contour range) decreases with the increase of Hc. The 90% concentration contour near the opening moves upward in the vertical direction with increasing wall depth and closer to the cutoff wall in the horizontal direction. As Hc increases, the 90% concentration contour on the right side of the opening moves upward, the position of the 50% concentration contour remains almost unchanged, and the position of the 10% concentration contour moves downward. The area of the nitrate mixing zone on the right side of the opening changes significantly with the increase of Hc, and the area of the mixing zone increases with the increase of Hc. Figure 10a and b demonstrate the effect of Hc values on nitrate accumulation. The variation curves of TNM and VNM follow a linear increase with increasing Hc. The TNM values

for cutoff wall depths of 9 m, 11 m, 13 m, 15 m, and 17 m were 27.48%, 31.69%, 36.10%, 40.10%, and 43.68%, respectively, corresponding to VNM of 24.62%, 28.61%, 32.88%, 37.13%, and 41.30%, with growth rates of about 2.03% and 2.09%, respectively. Comparing the effect of subsurface dam height on nitrate accumulation, it can be observed that the changes in TNM and VNM values are more significant when the depth of the cutoff wall is increased compared to the change in subsurface dam height.

SWI control performance

Figure 9 illustrates the salinity distribution under different cutoff wall depth conditions at the steady state. As shown in Fig. 9, barrier with varying Hc values can entirely control the SWI, and the mixing zone area after SWI stabilization significantly reduces compared to that before MPB installation. The variation process of R_M and R_S with time for different cutoff wall depths is presented in Fig. 10c and d. When the cutoff wall depth was large, the R_M values showed rapid growth, such as the saltwater removal rate exceeding 0.9 on day 600 for the first 600 days at $Hc = 17$ m. As the cutoff wall depth decreased, the growth rate of R_M decreased. For example, after 600 days of MPB installation, the R_M values for cutoff wall depths of 17 m, 15 m, 13 m, 11 m, and 9 m were 0.91, 0.83, 0.67, 0.53, and 0.44, respectively. This suggests that the efficiency of residual saltwater removal by MPB decreases with decreasing Hc. The time for complete removal of residual saltwater increases with decreasing cutoff wall depth, and the time for complete removal of residual saltwater is 1750, 2050, 3100, 4650, and 5900 days for cutoff wall depths of 17 m, 15 m, 13 m, 11 m, and 9 m, respectively. The variation pattern of R_S values is similar to that of R_M, where R_S values increase with time and eventually reach stability. The rate of increase of R_S increases with increasing Hc, and the elapsed time for the salt toe to reach the location of the subsurface dam decreases with increasing Hc. Combining Figs. 8 and 10, it is evident that the effect of the change in cutoff wall depth on the R_L and R_M values is more significant than the change in the height of the subsurface dam, consistent with the findings of Gao et al. (2021).

Influences of MPB spacing

Previous studies have indicated that the location of subsurface dam may significantly impact the performance of barrier against SWI (Chang et al. 2019; Zheng et al. 2020; Fang et al. 2021) and affect the exchange of material from the aquifer to the ocean (Fang et al. 2023). In this subsection, we use case B as the base case for Hd, Hc, and different Ls to analyze the impact of MPB opening spacing Ls on nitrate accumulation in the aquifer and the control of saltwater wedge performance. Unlike the setup of Gao et al. (2021),

Fig. 9 Steady-state cross-sectional distributions of salinity, NO$_3$.$^-$ and DOC for MPB using different cutoff wall depths. The purple, green, and yellow colors indicate the concentration contours of 10%, 50%, and 90%, respectively. The white columns are the subsurface dam and cutoff wall of the MPB, which are 17 m and 25 m from the sea-side boundary, respectively. realistic scales are used for the length units in [m]
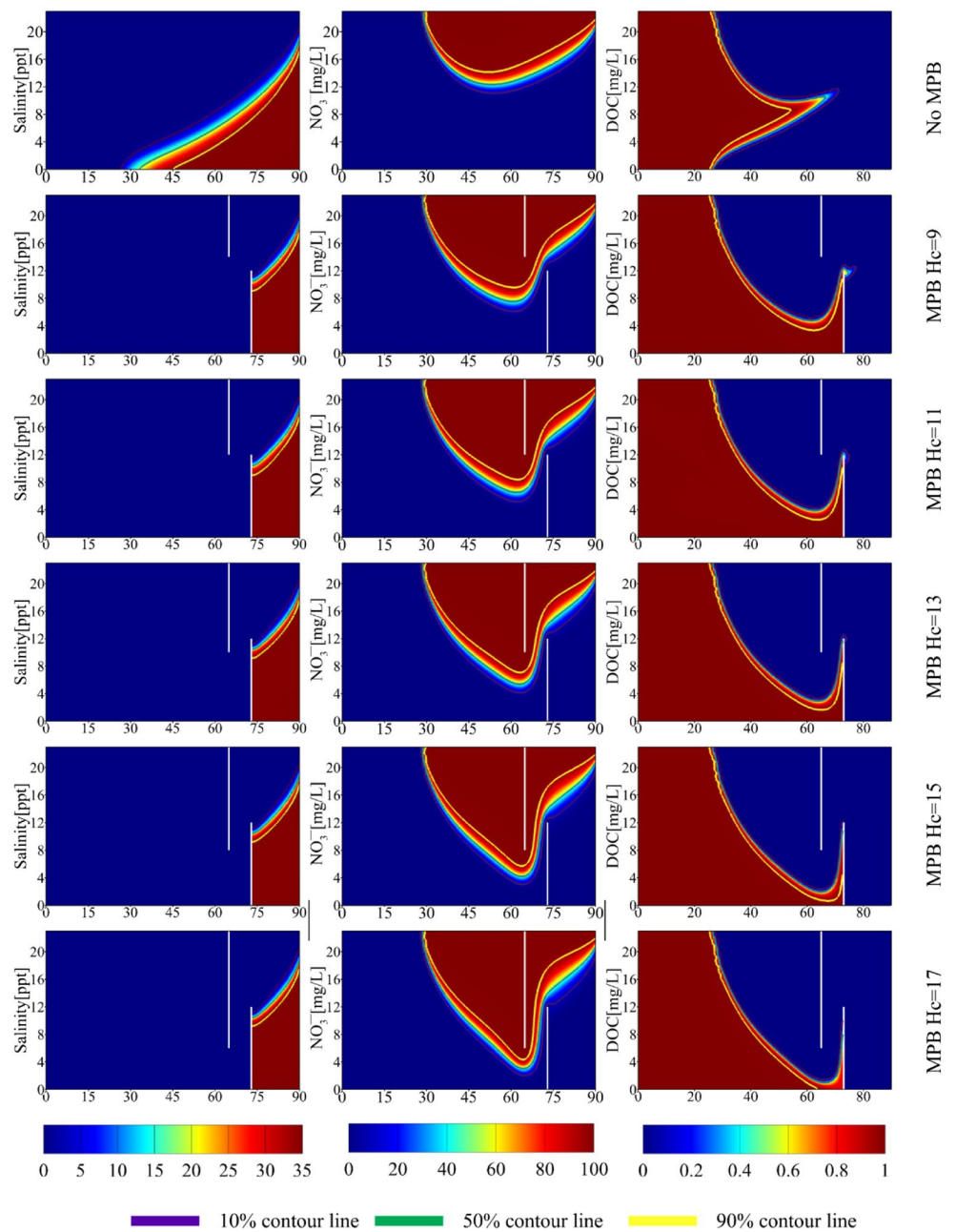
we define the MPB by the location of the cutoff wall instead of the location of the subsurface dam (Gao et al. 2021). We maintain the location of the cutoff wall constant and create two physical barrier spaced *Ls* by adjusting the location of the subsurface dam.

Nitrate accumulation

Figure 11 displays the steady-state distributions of nitrate and DOC for different MPB opening spacing conditions. As shown in Fig. 11, the impact of *Ls* on the NO$_3^-$ distribution on the left and right sides of the opening varied,

and generally, the change in NO$_3^-$ distribution on the right side was more significant than that on the left side. With an increase in *Ls*, the depth of the nitrate contaminated area to the left of the opening also increased, and the area of DOC distribution decreased slightly. However, the change was negligible. The area of the nitrate mixing zone (10 to 90% concentration contour range) on the left side of the opening did not exhibit significant alterations due to the increase in *Ls*. The 10%, 50%, and 90% concentration contours near the opening shifted downward with increasing spacing in the vertical direction and further away from the cutoff wall in the horizontal direction. As *Ls* increased, the

Fig. 10 **a** Variation of *TNM*, the accumulation rate of total nitrate mass in the aquifer, with depth of the cutoff wall, and *Hc* equals 0 corresponding to case A. **b** *VNM*, the increase rate of nitrate contaminated area in the aquifer, versus depth of the cutoff wall, and *Hc* equals 0 corresponding to case A. **c** The relationship between the rate of residual salt removal R_M after the barrier with different cutoff wall depths and time. **d** The variation of the rate of reduction of saltwater wedge length R_S with time using different cutoff wall depths
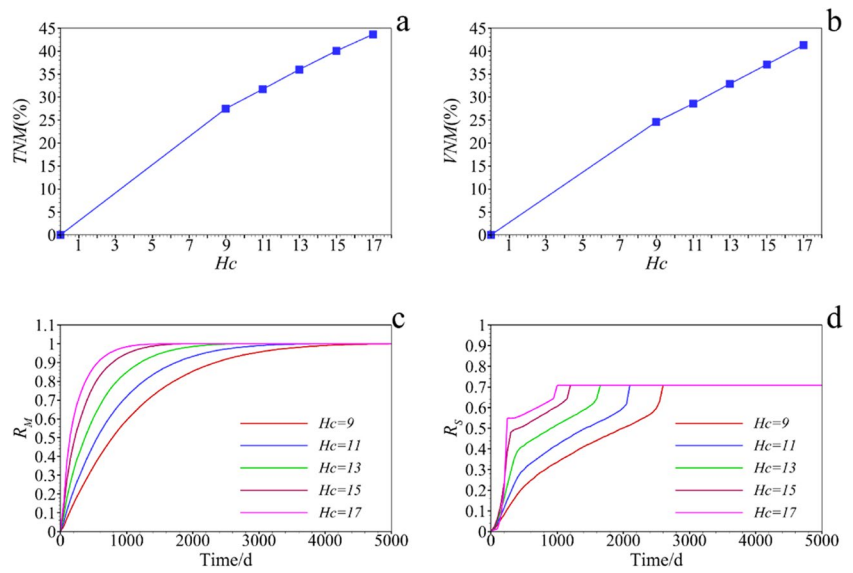
Fig. 11 Cross-sectional distribution of salinity, NO_3^- and DOC at different MPB opening spacing after reaching steady state. The purple, green, and yellow colors indicate the concentration contours of 10%, 50%, and 90%, respectively. The white columns are the subsurface dam and cutoff wall of the MPB, which are 21 m, 19 m, 17 m, and 15 m from the sea-side boundary, respectively. Realistic scales are used for the length units in [m]
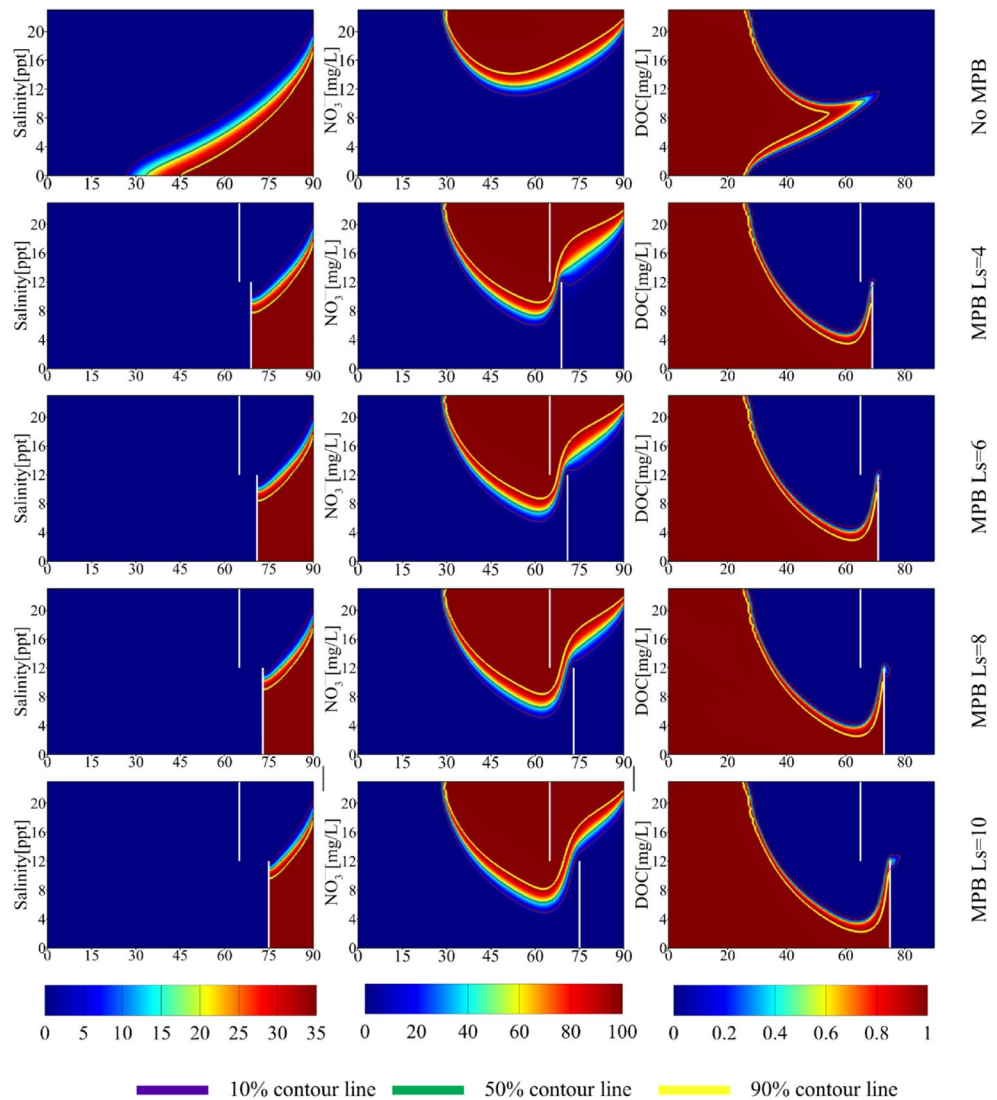
90% concentration contour on the right side of the opening moved down gradually, the position of the 50% concentration contour did not change significantly, and the position of the 10% concentration contour gradually moved up. The area of the nitrate mixing zone on the right side of the opening changed significantly due to the increase in Hc, and the area of the mixing zone decreased with the increase in Ls. Figure 12a and b illustrate the effect of the change in Ls value on nitrate enrichment. It can be observed that TNM and VNM are linearly and positively correlated with Ls, i.e., the larger the Ls, the larger the TNM and VNM. The TNM values corresponding to MPB spacing of 4 m, 6 m, 8 m, and 10 m are 25.32%, 28.57%, 31.69%, and 34.74%, respectively, and the corresponding VNM are 23.84%, 26.32%, 28.61%, and 31.22%, with TNM and VNM growth rates of approximately 1.57% and 1.23%, respectively.

SWI control performance

To evaluate the impact of Ls values on the performance of MPB-controlled SWI, we considered the formation of a steady-state saltwater wedge in case A and installing a physical barrier afterward. Figure 11 shows the SWI distribution after reaching a steady state, indicating that the area of the saltwater mixing zone significantly decreases after MPB installation. Additionally, the area of the saltwater mixing zone gradually decreases with an increase in Ls. The closer the subsurface dam is to the ocean boundary (i.e., the larger the Ls), the closer the low salinity mixing zone at the location of the subsurface dam is to the top part of the dam. The corresponding M_0 values are 5228.2 kg, 5840.5 kg, 6498.4 kg, and 7204.7 kg when the spacing between the cutoff wall and the subsurface dam is equal to 4 m, 6 m, 8 m, and 10 m, respectively, but the

initial saltwater wedge L_0 value within the aquifer is the same at 57.2 m.

Figure 12c illustrates the R_M course over time for different Ls values. During the first 600 days, the post-dam saltwater removal rate increased rapidly with time for all MPB opening spacings. Then, it underwent a long period of slow increase, during which the growth rate of R_M continuously decreased until all saltwater was removed ($R_M = 1$). The R_M change curves for $Ls = 4$ and $Ls = 6$ were almost identical. At the beginning of saline wedge removal (first 600 days), there was no significant difference in the R_M change curves for $Ls = 4$, $Ls = 6$, and $Ls = 8$. $Ls = 8$ and $Ls = 10$ exhibited a longer slow-rise period compared to $Ls = 6$ and $Ls = 4$, with the longest slow-rise period for $Ls = 10$. The complete removal times of residual saltwater for MPB spacing of 4 m, 6 m, 8 m, and 10 m were 4400, 4400, 4650, and 5100 days, respectively. This is mainly due to larger Ls values trapping a greater total amount of saltwater behind the dam. Figure 12d presents the variation of R_S with time for different Ls values. All R_S values increased with time and eventually reached stability. During the first 400 days, R_S values increased the fastest for $Ls = 10$. The overall increase in R_S values during this period was characterized by a decreasing rate of increase with decreasing Ls. The rate of increase of R_S values was almost the same for different Ls cases during the phase from day 400 to day 2000. There were some differences in the time for R_S to reach stability for different Ls cases. When $Ls = 4$ and $Ls = 6$, the time for both R_S values to reach stability was almost the same, 1900 and 1950 days, respectively. The time for R_S to reach stability was longer for $Ls = 8$ and 10, 2100 and 2300 days, respectively. When the saltwater can be completely removed behind the dam, the length of the stabilized saltwater wedge is related to the location of the subsurface dam, and different Ls values lead to different

Fig. 12 **a** Variation of *TNM*, the accumulation rate of total nitrate mass, with MPB opening spacing *Ls*. **b** *VNM*, the increase rate of nitrate contaminated area, versus MPB opening spacing *Ls*. **c** The relationship between R_M, the rate of residual salt removal after the barrier with different *Ls*, and time. **d** The variation process of R_S, the rate of reduction of saltwater wedge length with time using different *Ls*
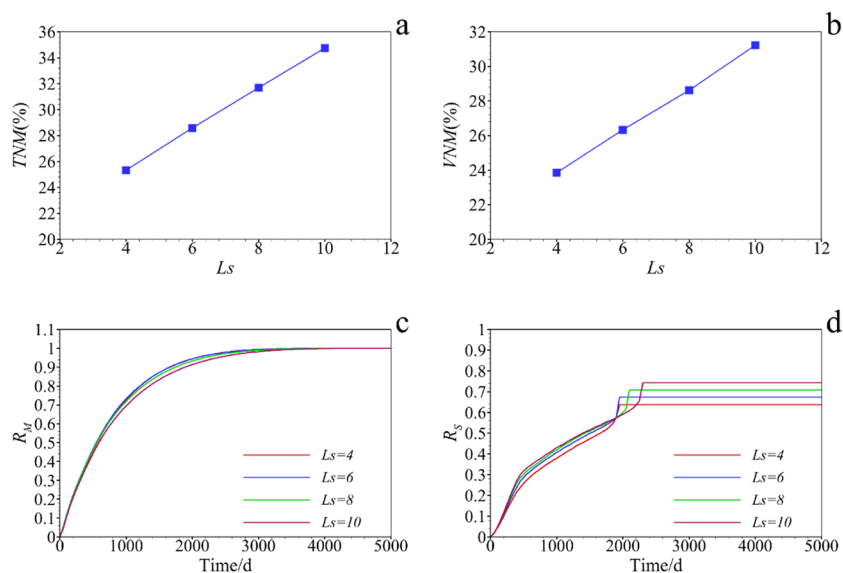
saltwater wedge setback distances. Therefore, the stabilized R_S value increases with an increase in *Ls*.

Comparison with single physical barrier

We compared MPB with single subsurface dam and cutoff wall to evaluate the differences between MPB and single physical barrier in controlling SWI and nitrate pollution enrichment. We assessed the capability of physical barrier to control SWI using R_M and R_S, and analyzed the effect of various physical barrier on the degree of nitrate contamination in the aquifer using *TNM* and *VNM*.

Comparison of MPB and subsurface dam

A comparative analysis of MPB with subsurface dam at different dam heights was performed by adjusting the *Hd* values based on the baseline case (Fig. 13). From Fig. 13a and b, it is evident that both *TNM* and *VNM* of the MPB are significantly higher than those of the subsurface dam due to the nitrate enrichment exacerbated by the presence of the cutoff wall. The relationship between *TNM* and *Hd* under subsurface dam conditions is consistent with the findings of Sun et al. (2021), indicating that anomalously low *TNM* values occur when the subsurface dam fails to control SWI, and after *Hd* exceeds the minimum effective dam height, *TNM* gradually decreases with an increase in *Hd*. The relationship between *VNM*, *TNM* and dam height for both shows an increasing and then decreasing pattern with an increase in *Hd*. Specifically, *TNM* and *VNM* increase with an increase in *Hd* when *Hd* is less than 10 m. After *Hd* exceeds 10 m, *TNM* and *VNM* gradually

decrease with an increase in *Hd*. The *TNM* values for the MPB case at dam heights of 8 m, 10 m, 12 m, 14 m, and 16 m were 30.02%, 33.58%, 31.69%, 29.31%, and 26.77%, respectively, corresponding to a *VNM* of 27.35%, 30.07%, 28.61%, 27.02%, and 25.69%, respectively. The *TNM* values for subsurface dam at the corresponding dam heights were 3.37%, 19.51%, 17.51%, 14.41%, and 10.80%, with corresponding *VNM* of 2.85%, 17.45%, 15.67%, 13.09%, and 10.39%, respectively. In other words, the enrichment effect of MPB on nitrate pollution is 14 to 27% higher than that of a single subsurface dam.

The MPB outperforms the subsurface dam significantly in terms of SWI control. From Fig. 13c and d, it is evident that both the MPB and the subsurface dam fail to control SWI effectively for *Hd* = 8, but there is a significant difference between them. When the R_M and R_S values reached stability, the MPB had significantly higher R_M and R_S values of 0.84 and 0.48 compared to the single dam's values of 0.21 and 0.07, respectively, indicating that the presence of the cutoff wall accelerated the saltwater removal rate. Both MPB and subsurface dam follow the characteristic that the rate of saltwater removal behind the dam decreases as *Hd* increases, which is consistent with the findings of Gao et al. (2021). The R_M and R_S rise rates were greater for MPB than for subsurface dam conditions at different dam heights. For the MPB case, saltwater removal times were 4050, 4650, 4850, and 5000 days for 10 m, 12 m, 14 m, and 16 m subsurface dam heights, respectively. The saltwater removal times for subsurface dam at the corresponding dam heights were 7900, 8600, 9650, and 10,700 days, respectively. Thus, the MPB removes saltwater 46 to 53% faster than the subsurface dam. Notably,

Fig. 13 Comparison of the performance of MPB and single subsurface dam at different dam heights. **a** Total nitrate mass accumulation rate *TNM*, and *Hd* equals 0 corresponding to case A. **b** Increase rate of nitrate contaminated area *VNM*, and *Hd* equals 0 corresponding to case A. **c** Residual salt removal rate R_M after the barrier versus time. **d** Variation process of saltwater wedge length reduction rate R_S with time
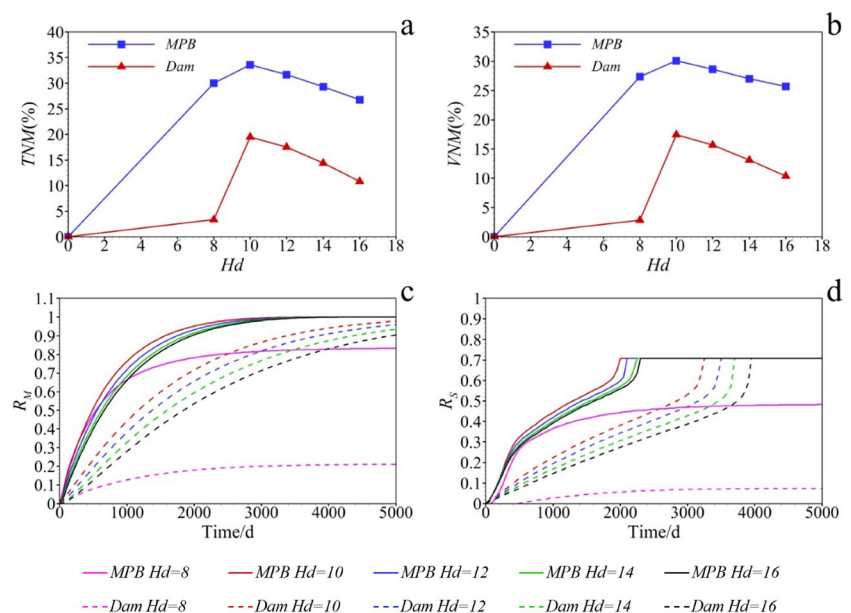
even when the dam height of the MPB is larger, its SWI control performance is still superior to that of the subsurface dam with a lower dam height. For instance, when the *Hd* of the MPB is 16 m and that of the subsurface dam is 10 m, at day 1000, the R_M and R_S of MPB are 0.66 and 0.39, respectively, while those of the subsurface dam are 0.44 and 0.22.

Comparison of MPB and cutoff wall

Based on the baseline case, the MPB was compared with a single cutoff wall at different cutoff wall depths by adjusting the *Hc* value (Fig. 14). It should be noted that we placed the cutoff wall at the same location as the cutoff wall in the MPB, while M_0 was calculated using the residual saltwater behind the location of the subsurface dam in the MPB.

Figure 14a and b reveal that the nitrate enrichment and contaminated area of both MPB and cutoff wall increased gradually with increasing depth of the cutoff wall, following a linear trend. Although both *TNM* and *VNM* of MPB are greater than those of the cutoff wall, the difference between them diminishes as the depth of the cutoff wall increases, indicating that the cutoff wall's contribution to nitrate enrichment increases with greater depth. The *TNM* values for the cutoff wall depths of 9 m, 11 m, 13 m, 15 m, and 17 m in the MPB case were 27.48%, 31.69%, 36.10%, 40.10%, and 43.68%, respectively, with corresponding *VNM* values of 24.62%, 28.61%, 32.88%, 37.13%, and 41.30%. For the cutoff wall, *TNM* values at corresponding depths were 3.37%, 19.51%, 17.51%, 14.41%, and 10.80%, with corresponding *VNM* values of 14.35%, 21.06%, 28.15%, 34.81%, and 40.61%, respectively. Consequently, the nitrate

enrichment effect of MPB is 2 to 12% higher than that of a single cutoff wall.

Figure 14c and d demonstrate that increasing wall depth improves the control performance of both the cutoff wall and MPB for SWI, with the R_M and R_S values of the cutoff wall reaching stability sooner than the MPB. However, the R_M and R_S values of MPB can reach 1.0 and 0.71, respectively, while the highest values for the cutoff wall are only 0.82 and 0.54, respectively, and even the stable R_M and R_S values are only 0.43 and 0.27 when the wall depth is small. This indicates that the MPB can increase the retreat distance of the saltwater wedge, decrease contamination by brackish water in the aquifer, and provide better protection for underground freshwater resources. The stable R_M and R_M values for various wall depths reveal that the MPB controls SWI more efficiently than the cutoff wall, with an improvement of 16 to 57%.

Comparing the MPB to a single physical barrier, the study found that the MPB was more prone to NO_3^- accumulation than the subsurface dam and the cutoff wall, with the obstructive effect of the cutoff wall being the primary cause of the increased NO_3^- pollutants. However, conventional physical barrier is inadequate for controlling SWI. Subsurface dam is unable to rapidly remove saltwater behind the dam, particularly at greater heights, and the removal of saltwater wedges can take decades. Cutoff wall is unable to stably and effectively control the intrusion distance of saltwater. In contrast, the MPB maintains high efficiency in removing saltwater and possesses stable and effective control performance of saltwater wedges, even at high dam heights or shallow cutoff wall depths.

It is clear that physical barrier is conflicting in controlling saltwater intrusion and nitrate pollution in the

Fig. 14 Comparison of the performance of MPB and single cutoff wall under different cutoff wall depth conditions. **a** Total nitrate mass accumulation rate *TNM*, and *Hc* equals 0 corresponding to case A. **b** Increase rate of nitrate contaminated area *VNM*, and *Hc* equals 0 corresponding to case A. **c** Residual salt removal rate R_M versus time. **d** Variation process of saltwater wedge length reduction rate R_S with time
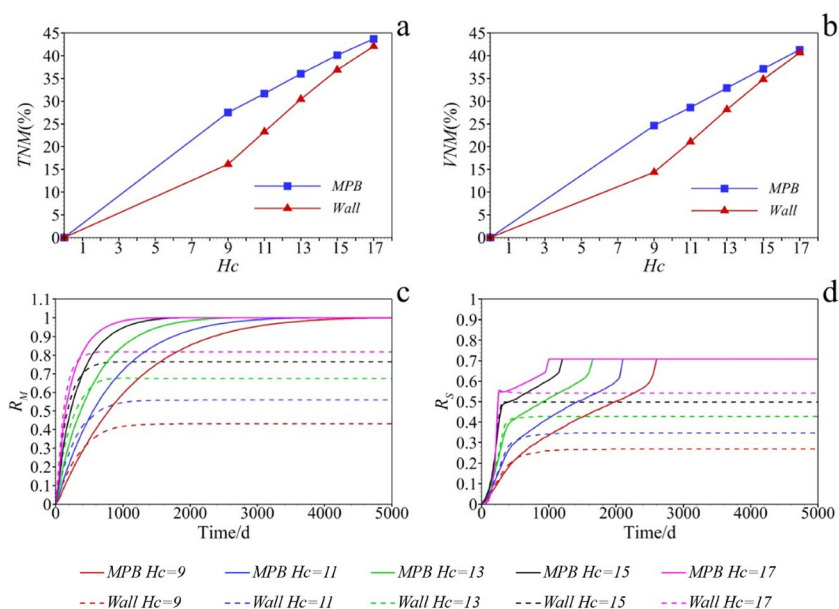
aquifer. For this contradiction, Sun et al. (2021) concluded that although the accumulation of NO_3^- caused by subsurface dam is small, the removal of residual saltwater wedges after the dam is slow, and for areas where SWI has occurred, cutoff wall measures should be used in preference to the use of subsurface dam. Our study shows that when the depth of the wall is large, the cutoff wall is still weaker than MPB in controlling the saltwater wedge, while the degree of NO_3^- pollution accumulation generated is very close to that of MPB. Therefore, we believe that for areas where severe SWI exists, the use of MPB can strike a relative balance between accelerated aquifer saltwater removal and control of nitrate pollution. For areas where SWI has not occurred, subsurface dam should be used, which can provide good prevention of SWI while reducing the accumulation of nitrate pollution.

Conclusion

This study aimed to evaluate the performance of an MPB against SWI and its impact on nitrate pollution accumulation using numerical simulation. Through univariate analysis, we assessed how the performance of the MPB in controlling SWI and nitrate pollution accumulation is affected by subsurface dam height, cutoff wall depth, and opening spacing. We compared the differences between MPB and single physical barrier to assess the applicability of these three types of physical barrier. Our study draws the following conclusions:

1. The installation of MPB resulted in an increase in the total nitrate mass and the area of nitrate contamination in the aquifer.
2. In the MPB structure, the degree of nitrate enrichment did not follow a monotonous pattern as the dam height increased. As the subsurface dam height (Hd) increased from 8 to 16 m, the *TNM* and *VNM* values initially showed an increase (from 30.02 to 33.58% and from 27.35 to 30.07%, respectively), followed by a gradual decrease (from 33.58 to 26.77% and from 30.07 to 25.69%, respectively). If the dam height of the subsurface dam was too low, the MPB would not be able to effectively prevent and control SWI. Conversely, with an increase in dam height, the removal efficiency of saltwater behind the dam decreased. The degree of nitrate enrichment was directly proportional to the depth of the cutoff wall. *TNM* increased from 27.48 to 43.68%, and *VNM* increased from 24.62 to 41.30% as *Hc* increased from 9 to 17 m. Additionally, with an increase in *Hc*, the removal efficiency of post-dam saltwater improved, and the removal time

decreased from 5900 to 1750 days. *TNM* and *VNM* showed a linear and positive correlation with the MPB opening spacing, and the stabilized saline wedge length decreased with an increase in *Ls*.

3. A contradictory relationship was observed between accelerated SWI removal and reduced nitrate pollution. MPB exhibits significant advantages in controlling SWI efficiency, which is 46 to 53% and 16 to 57% higher than that of conventional subsurface dam and cutoff wall, respectively. Nonetheless, the use of MPB results in more severe nitrate accumulation, which is 14 to 27% and 2 to 12% higher than that of subsurface dam and cutoff wall, respectively. In aquifers where SWI has occurred, MPB can be employed to strike a relative balance between improving SWI control efficiency and controlling nitrate contamination. Conversely, in areas where SWI does not occur, subsurface dam can effectively prevent SWI while reducing the accumulation of nitrate pollution.

In our study, we assumed that the aquifer is homogenous and isotropic, and we did not consider the tidal fluctuations of the ocean. Real-life aquifers are complex, possibly layered, anisotropic, and influenced by tides and waves. As a result, the process of nitrate accumulation and SWI removal is more complicated, and the current model needs refinement to accurately reflect such complexities. Our study provides valuable physical mechanisms and laws that can aid in the practical application of MPB and traditional physical barrier. Policy makers should evaluate the most appropriate physical barrier for their specific situation and strike a relative balance between SWI control efficiency and nitrate pollution.

Declarations

Ethics approval Not applicable.

Consent to participate Not applicable.

Consent for publication Not applicable.

Competing interests The authors declare no competing interests.

References

Abarca E, Karam HN, Hemond HF, Harvey CF (2013) Transient groundwater dynamics in a coastal aquifer: The effects of tides, the lunar cycle, and the beach profile. Water Resour Res 49:2473–2488. https://doi.org/10.1002/wrcr.20075

Abdoulhalik A, Ahmed AA (2017) The effectiveness of cutoff walls to control saltwater intrusion in multi-layered coastal aquifers: Experimental and numerical study. J Environ Manage 199:62–73. https://doi.org/10.1016/j.jenvman.2017.05.040

Abdoulhalik A, Ashraf AA (2017) How does layered heterogeneity affect the ability of subsurface dam to clean up coastal aquifers contaminated with seawater intrusion. J Hydrol 553:708–721. https://doi.org/10.1016/j.jhydrol.2017.08.044

Abdoulhalik A, Ahmed AA, Hamill GA (2017) A new physical barrier system for seawater intrusion control. J Hydrol 549:416–427. https://doi.org/10.1016/j.jhydrol.2017.04.005

Anwar N, Robinson C, Barry DA (2014) Influence of tides and waves on the fate of nutrients in a nearshore aquifer: Numerical simulations. Adv Water Resour 73:203–213. https://doi.org/10.1016/j.advwatres.2014.08.015

Bardini L, Boano F, Cardenas MB, Revelli R, Ridolfi L (2012) Nutrient cycling in bedform induced hyporheic zones. Geochim Cosmochim Acta 84:47–61. https://doi.org/10.1016/j.gca.2012.01.025

Board OS, National Research Council (2007) Mitigating shore erosion along sheltered coasts. National Academies Press. https://doi.org/10.17226/11764

Cardenas MB, Bennett PC, Zamora PB, Befus KM, Rodolfo RS, Cabria HB, Lapus MR (2015) Devastation of aquifers from tsunami-like storm surge by Supertyphoon Haiyan. Geophys Res Lett 42(8):2844–2851. https://doi.org/10.1002/2015GL063418

Chang Q, Zheng T, Zheng X, Zhang B, Sun Q, Walther M (2019) Effect of subsurface dam on saltwater intrusion and fresh groundwater discharge. J Hydrol 576:508–519. https://doi.org/10.1016/j.jhydrol.2019.06.060

Chui TFM, Freyberg DL (2009) Implementing hydrologic boundary conditions in a multiphysics model. J Hydrol Eng 14(12):1374–1377. https://doi.org/10.1061/(ASCE)HE.1943-5584.0000113

Cui Z, Welty C, Maxwell RM (2014) Modeling nitrogen transport and transformation in aquifers using a particle-tracking approach. Comput Geosci 70:1–14. https://doi.org/10.1016/j.cageo.2014.05.005

Ebeling P, Händel F, Walther M (2019) Potential of mixed hydraulic barrier to remediate seawater intrusion. Sci Total Environ 693:133478. https://doi.org/10.1016/j.scitotenv.2019.07.284

Fang Y, Zheng T, Zheng X, Peng H, Wang H, Xin J, Zhang B (2020) Assessment of the hydrodynamics role for groundwater quality using an integration of GIS, water quality index and multivariate statistical techniques. J Environ Manag 273:111185. https://doi.org/10.1016/j.jenvman.2020.111185

Fang Y, Zheng T, Wang H, Guan R, Zheng X, Walther M (2021) Experimental and numerical evidence on the influence of tidal activity on the effectiveness of subsurface dams. J Hydrol 603:127149. https://doi.org/10.1016/j.jhydrol.2021.127149

Fang Y, Zheng T, Wang H, Zheng X, Walther M (2022) Nitrate transport behavior behind subsurface dam under varying hydrological conditions. Sci Total Environ 838:155903. https://doi.org/10.1016/j.scitotenv.2022.155903

Fang Y, Qian J, Zheng T, Wang H, Zheng X, Walther M (2023) Submarine groundwater discharge in response to the construction of subsurface physical barriers in coastal aquifers. J Hydrol 617:129010. https://doi.org/10.1016/j.jhydrol.2022.129010

Gao M, Zheng T, Chang Q, Zheng X, Walther M (2021) Effects of mixed physical barrier on residual saltwater removal and groundwater discharge in coastal aquifers. Hydrol Process 35(7):e14263. https://doi.org/10.1002/hyp.14263

Gao S, Zheng T, Zheng X, Walther M (2022) Influence of layered heterogeneity on nitrate accumulation induced by cut-off wall in coastal aquifers. J Hydrol 609:127722. https://doi.org/10.1016/j.jhydrol.2022.127722

Gao C, Kong J, Zhou L, Shen C, Wang J (2023) Macropores and burial of dissolved organic matter affect nitrate removal in intertidal aquifers. J Hydrol 617:129011. https://doi.org/10.1016/j.jhydrol.2022.129011

Gibert O, Assal A, Devlin H, Elliot T, Kalin RM (2019) Performance of a field-scale biological permeable reactive barrier for in-situ remediation of nitrate-contaminated groundwater. Sci Total Environ 659:211–220. https://doi.org/10.1016/j.scitotenv.2018.12.340

Heiss JW, Post VE, Laattoe T, Russoniello CJ, Michael HA (2017) Physical controls on biogeochemical processes in intertidal zones of beach aquifers. Water Resour Res 53(11):9225–9244. https://doi.org/10.1002/2017WR021110

Hu R, Zheng X, Zheng T, Xin J, Wang H, Sun Q (2019) Effects of carbon availability in a woody carbon source on its nitrate removal behavior in solid-phase denitrification. J Environ Manag 246:832–839. https://doi.org/10.1016/j.jenvman.2019.06.057

Jang E, He W, Savoy HM, Dietrich P, Kolditz O, Rubin Y, Schüth C, Kalbacher T (2017) Identifying the influential aquifer heterogeneity factor on nitrate reduction processes by numerical simulation. Adv Water Resour 99:38–52. https://doi.org/10.1016/j.advwatres.2016.11.007

Japan Green Resources Agency (2004) Technical Reference for Effective Groundwater Development (p. 325). Saiwai-ku, Kawasaki, Kanagawa Prefecture, Japan: Japan Green Resources Agency. Retrieved from https://www.jircas.go.jp/en/file/67536/download?token=WYgbdYBZ

Kang P, Xu S (2017) The impact of an underground cut-off wall on nutrient dynamics in groundwater in the lower Wang River watershed, China. Isot Environ Health Stud 53(1):36–53. https://doi.org/10.1080/10256016.2016.1186670

Ke S, Chen J, Zheng X (2021) Influence of the subsurface physical barrier on nitrate contamination and seawater intrusion in an unconfined aquifer. Environ Pollut 284:117528. https://doi.org/10.1016/j.envpol.2021.117528

Lu C, Luo J (2010) Dynamics of freshwater-seawater mixing zone development in dual-domain formations. Water Resour Res 46(11):1–6. https://doi.org/10.1029/2010WR009344

Lu C, Tian H (2017) Global nitrogen and phosphorus fertilizer use for agriculture production in the past half century: shifted hot spots and nutrient imbalance. Earth Syst Sci Data 9:181–192. https://doi.org/10.5194/essd-9-181-2017

Lu C, Kitanidis PK, Luo J (2009) Effects of kinetic mass transfer and transient flow conditions on widening mixing zones in coastal aquifers. Water Resour Res 45(12):1–17. https://doi.org/10.1029/2008WR007643

Lu C, Xin P, Kong J, Li L, Luo J (2016) Analytical solutions of seawater intrusion in sloping confined and unconfined coastal aquifers. Water Resour Res 52(9):6989–7004. https://doi.org/10.1002/2016WR019101

Lu C, Shi W, Xin P, Wu J, Werner AD (2017) Replenishing an unconfined coastal aquifer to control seawater intrusion: injection or infiltration? Water Resour Res 53(6):4775–4786. https://doi.org/10.1002/2016WR019625

Luyun R, Momii K, Nakagawa K (2009) Laboratory-scale saltwater behavior due to subsurface cutoff wall. J Hydrol 377(3–4):227–236. https://doi.org/10.1016/j.jhydrol.2009.08.019

McAnally WH, Pritchard DW (1997) Salinity control in Mississippi river under drought flows. J Waterw Port Coastal Ocean Eng 123(1):34–40. https://doi.org/10.1061/(ASCE)0733-950X(1997)123:1(34)

Nai H, Xin J, Liu Y, Zheng X, Lin Z (2020) Distribution and molecular chemodiversity of dissolved organic nitrogen in the vadose

zone-groundwater system of a fluvial plain, northern China: implications for understanding its loss pathway to groundwater. Sci Total Environ 723:137928. https://doi.org/10.1016/j.scitotenv.2020.137928

Nawa N, Miyazaki K (2009) The analysis of saltwater intrusion through Komesu underground dam and water quality management for salinity. Paddy Water Environ 7:71–82. https://doi.org/10.1007/s10333-009-0154-1

Reeves HW, Thibodeau PM, Underwood RG, Gardner LR (2000) Incorporation of total stress changes into the ground water model SUTRA. Groundwater 38(1):89–98. https://doi.org/10.1111/j.1745-6584.2000.tb00205.x

Rozell DJ, Wong TF (2010) Effects of climate change on groundwater resources at Shelter Island, New York State, USA. Hydrogeol J 18(7):1657–1665. https://doi.org/10.1007/s10040-010-0615-z

Senthilkumar M, Elango L (2011) Modelling the impact of a subsurface barrier on groundwater flow in the lower Palar River basin, southern India. Hydrogeol J 19(4):917–928. https://doi.org/10.1007/s10040-011-0735-0

Shen C, Zhang C, Kong J, Xin P, Lu C, Zhao Z, Li L (2019) Solute transport influenced by unstable flow in beach aquifers. Adv Water Resour 125:68–81. https://doi.org/10.1016/j.advwatres.2019.01.009

Shen Y, Xin P, Yu X (2020) Combined effect of cutoff wall and tides on groundwater flow and salinity distribution in coastal unconfined aquifers. J Hydrol 581:124444. https://doi.org/10.1016/j.jhydrol.2019.124444

Shoushtari SM, Nielsen P, Cartwright N, Perrochet P (2015) Periodic seepage face formation and water pressure distribution along a vertical boundary of an aquifer. J Hydrol 523:24–33. https://doi.org/10.1016/j.jhydrol.2015.01.027

Sun Q, Zheng T, Zheng X, Chang Q, Walther M (2019) Influence of a subsurface cut-off wall on nitrate contamination in an unconfined aquifer. J Hydrol 575:234–243. https://doi.org/10.1016/j.jhydrol.2019.05.030

Sun Q, Zheng T, Zheng X, Walther M (2021) Effectiveness and comparison of physical barrier on seawater intrusion and nitrate accumulation in upstream aquifers. J Contam Hydrol 243:103913. https://doi.org/10.1016/j.jconhyd.2021.103913

Torres-Martínez JA, Mora A, Mahlknecht J, Daesslé LW, Cervantes-Avilés PA, Ledesma-Ruiz R (2021) Estimation of nitrate pollution sources and transformations in groundwater of an intensive livestock-agricultural area (Comarca Lagunera), combining major ions, stable isotopes and MixSIAR model. Environ Pollut 269:115445. https://doi.org/10.1016/j.envpol.2020.115445

Van Genuchten MT (1980) A closed-form equation for predicting the hydraulic conductivity of unsaturated soils. Soil Sci Soc Am J 44(5):892–898. https://doi.org/10.2136/sssaj1980.03615995004400050002x

Voss CI, Souza WR (1987) Variable density flow and solute transport simulation of regional aquifers containing a narrow freshwater-saltwater transition zone. Water Resour Res 23(10):1851–1866. https://doi.org/10.1029/WR023i010p01851

Walther M, Graf T, Kolditz O, Liedl R, Post VE (2017) How significant is the slope of the sea-side boundary for modelling seawater intrusion in coastal aquifers? J Hydrol 551:648–659. https://doi.org/10.1016/j.jhydrol.2017.02.031

Wang H, Xin J, Zheng X, Li M, Fang Y, Zheng T (2020) Clogging evolution in porous media under the coexistence of suspended particles and bacteria: Insights into the mechanisms and implications for groundwater recharge. J Hydrol 582:124554. https://doi.org/10.1016/j.jhydrol.2020.124554

Werner AD, Simmons CT (2009) Impact of sea-level rise on sea water intrusion in coastal aquifers. Groundwater 47(2):197–204. https://doi.org/10.1111/j.1745-6584.2008.00535.x

Werner AD, Bakker M, Post VE, Vandenbohede A, Lu C, Ataie-Ashtiani B, Simmons CT, Barry DA (2013) Seawater intrusion processes, investigation and management: Recent advances and future challenges. Adv Water Resour 51:3–26. https://doi.org/10.1016/j.advwatres.2012.03.004

Wilson AM, Gardner LR (2006) Tidally driven groundwater flow and solute exchange in a marsh: numerical simulations. Water Resour Res, 42(1). https://doi.org/10.1029/2005WR004302.

Wu H, Lu C, Kong J, Werner AD (2020) Preventing seawater intrusion and enhancing safe extraction using finite-length, impermeable subsurface barrier: 3D analysis. Water Resources Research 56(11):e2020WR027792. https://doi.org/10.1029/2020WR027792

Xin J, Liu Y, Chen F, Duan Y, Wei G, Zheng X, Li M (2019) The missing nitrogen pieces: a critical review on the distribution, transformation, and budget of nitrogen in the vadose zone-groundwater system. Water Res 165:114977. https://doi.org/10.1016/j.watres.2019.114977

Xin J, Wang Y, Shen Z, Liu Y, Wang H, Zheng X (2021) Critical review of measures and decision support tools for groundwater nitrate management: a surface-to-groundwater profile perspective. J Hydrol 598:126386. https://doi.org/10.1016/j.jhydrol.2021.126386

Yan M, Lu C, Werner AD, Luo J (2021) Analytical, experimental, and numerical investigation of partially penetrating barriers for expanding island freshwater lenses. Water Resour Res 57:e2020WR028386. https://doi.org/10.1029/2020WR028386

Yoshimoto S, Tsuchihara T, Ishida S, Imaizumi M (2013) Development of a numerical model for nitrates in groundwater in the reservoir area of the Komesu subsurface dam, Okinawa, Japan. Environ Earth Sci 70:2061–2077. https://doi.org/10.1007/s12665-011-1356-6

Zambito Marsala R, Capri E, Russo E, Barazzoni L, Peroncini E, De Crema M, Carrey Labarta R, Otero N, Colla R, Calliera M, Fontanella MC, Suciu NA (2021) Influence of nitrogen-based fertilization on nitrates occurrence in groundwater of hilly vineyards. Sci Total Environ 766:144512. https://doi.org/10.1016/j.scitotenv.2020.144512

Zang Y, Li M (2021) Numerical assessment of compressed air injection for mitigating seawater intrusion in a coastal unconfined aquifer. J Hydrol 595:125964. https://doi.org/10.1016/j.jhydrol.2021.125964

Zhang W, Bai Y, Ruan X, Yin L (2019) The biological denitrification coupled with chemical reduction for groundwater nitrate remediation via using SCCMs as carbon source. Chemosphere 234:89–97. https://doi.org/10.1016/j.chemosphere.2019.06.005

Zhang B, Zheng T, Zheng X, Walther M (2021) Utilization of pit lake on the cleaning process of residual saltwater in unconfined coastal aquifers. Sci Total Environ 770:144670. https://doi.org/10.1016/j.scitotenv.2020.144670

Zheng T, Zheng X, Chang Q, Zhan H, Walther M (2020) Timescale and effectiveness of residual saltwater desalinization behind subsurface dam in an unconfined aquifer. Water Resour Res 57:1–18. https://doi.org/10.1029/2020wr028493